

## Chapter 4    **The Vertical Distribution of Dust in the Martian Atmosphere during Northern Spring and Summer**

### **4.1 Introduction**

Because it is strongly radiatively active and highly temporally and spatially variable in its abundance, suspended dust is the martian atmosphere's most meteorologically important component. On this account, observations of its optical properties and spatial and temporal variability have been a part of almost every major spacecraft mission sent to Mars. However, the information provided by these missions about the vertical distribution of atmospheric dust has been limited. Mariner 9 provided information about the vertical distribution of dust during global dust storm conditions [*Conrath, 1975; Anderson and Leovy, 1978*]. *Jaquin et al.* [1986] used Viking Orbiter limb imagery to investigate a reddish "continuous haze," which was interpreted to be more dust-rich than the "detached" water ice hazes observed above it. *Jaquin et al.* [1986] also determined that this continuous haze was seasonally and latitudinally variable in height. Observations of Tharsis by instruments on the Phobos spacecraft during early northern spring suggested that dust was well-mixed vertically below 25 km [*Chassefière et al., 1995*]. More recently, limb observations from the Thermal Emission Spectrometer (TES) on Mars Global Surveyor (MGS) have been used to retrieve vertical profiles of dust during global dust storm conditions [e.g., *Clancy et al., 2009*].

Measurements of the vertical distribution of dust in particular (as opposed to the column opacity) are relevant to two important problems of martian meteorology. First, dust has a significant effect on the general circulation of the martian atmosphere. Solar

radiation absorbed by dust during the daytime is a crucial source of diabatic heating to the lower atmosphere and thus may be one driver of the planet's vigorous principal meridional overturning circulation (PMOC) (sometimes called "the Hadley circulation") and a modifier of Mars's strong thermal tides (see *Zurek et al.* [1992] for discussion). By absorbing and emitting infrared radiation both day and night, dust, like water vapor on the Earth, either can limit or enhance the radiative cooling of the atmosphere to space. As a result, even relatively small amounts of dust in the atmosphere can influence the circulation by enhancing the static stability [*Haberle et al.*, 1982; *Schneider*, 1983].

The effects of dust on the circulation can be highly non-local. From Mariner 9 and later observations, it is known that the winter polar middle atmosphere of Mars is much warmer than would be expected from considerations of radiative equilibrium [*Leovy*, 1982]. Middle atmospheric temperatures over the south pole during northern winter observed by the Thermal Emission Spectrometer (TES) on Mars Global Surveyor (MGS) and Mars Climate Sounder (MCS) on Mars Reconnaissance Orbiter (MRO) are 10–30 K warmer than predicted by most Mars climate models [*Smith et al.*, 2001; *McCleese et al.*, 2008]. Modeling studies attribute middle atmospheric polar warming to adiabatic heating due to the downwelling of the PMOC and connect the intensity of PMOC downwelling to the amount of dust in the atmosphere and to the level and intensity of wave breaking in the middle atmosphere [*Haberle et al.*, 1982; *Schneider*, 1983; *Barnes*, 1990; *Haberle et al.*, 1993; *Forget et al.*, 1999; *Hartogh et al.*, 2007]. Basic considerations from theory, simple nearly inviscid axisymmetric circulation models [*Schneider*, 1983] and more sophisticated terrestrial models [*Rind and Rossow*, 1984; *Wang and Rossow*, 1998] suggest that the Hadley circulation of a planet is sensitive to the vertical distribution of

atmospheric heating. Thus, knowledge of the vertical distribution of dust in the atmosphere provides a key constraint for Mars General Circulation Models (GCMs), analogous to the constraint cloud observations provide for terrestrial GCMs.

Information about the vertical distribution of dust also can provide insights into the mechanisms by which dust enters and leaves the atmosphere. *Conrath* [1975], for instance, attributed the vertical distribution to the competing effects of sedimentation and vertically uniform vertical eddy diffusion. This simple picture has been complicated by (1) the possibility of additional removal processes such as the enhancement of sedimentation by the condensation of volatiles on dust particles (S.M. Nelli and J.R. Murphy, Interrelationship between the Dust and Water Cycles in the Martian Atmosphere: Numerical Modeling Studies, paper presented at the 200th Meeting of the American Astronomical Society, Albuquerque, NM, June 2002); (2) more detailed modeling of vertical transport above the boundary layer due to dynamical processes such as the thermal tides [*Wilson and Hamilton*, 1996]; (3) more detailed treatment of mixing within the boundary layer [*Taylor et al.*, 2007]; (4) explicit consideration of variability in dust size [*Kahre et al.*, 2008] and (5) consideration of particular dust sources such as mountain slopes [*Lee et al.*, 1982; *Rafkin et al.*, 2002] and dry convective helical vortices (“dust devils”) [*Kahre et al.*, 2006; *Cantor et al.*, 2006; *Greeley et al.*, 2006]. However, these processes have been investigated primarily by modeling constrained by both the limited observational information about the vertical distribution of dust and more widespread observations of modification of surface features by aeolian processes.

For the last 1.5 martian years, the Mars Climate Sounder (MCS) on Mars Reconnaissance Orbiter (MRO) has been making global, high signal to noise

observations of infrared radiance from Mars's limb (and some nadir and off-nadir observations as well) in nine broadband channels with varying sensitivity to dust, temperature, and other aerosol (see *McCleese et al.* [2007] for description of the instrument and observing strategy.) Simultaneous retrievals from MCS limb observations of temperature, dust, and water ice at moderate vertical resolution ( $\sim 5$  km) are now available [*Kleinböhl et al.*, 2009]. These retrievals provide an extensive dataset to investigate both the contribution of dust to both the vertical heating structure of the atmosphere and also dust lifting and transport processes.

In this study, I focus on the zonal average vertical dust distribution during martian northern summer,  $L_s=111^\circ$ — $177^\circ$  of Mars Year (MY) 28 (2006—2007), and martian northern spring and summer,  $L_s=0^\circ$ — $180^\circ$  of MY 29 (2007—2008). (For a discussion of the Mars Year convention used, see *Clancy et al.* [2000]). These periods have dense MCS retrieval coverage and (not coincidentally) mostly exclude the canonical “dust storm season” ( $L_s=161^\circ$ — $346^\circ$ ) classified by *Martin and Zurek* [1993] and thus might be called, “the clear season.” While general weather patterns during the clear season are thought to be highly repeatable, even in the wake of a global dust event [*Richardson*, 1998; *Wilson and Richardson*, 2000; *Cantor et al.*, 2002], recent work by *Smith* [2009] suggests that mid to late summer tropical dust activity may have considerable interannual variability. Therefore, I can test whether this variability is evident in the planetary-scale vertical dust distribution. I also can investigate the contribution of dust to the vertical heating structure during the season in which *McCleese et al.* [2008] infer an unexpectedly intense PMOC.

In Chapter 4.2, I describe the retrieval dataset used and its limitations, which circumscribe this investigation. In Chapter 4.3, I present a new scheme for representing

vertical dust distributions in a compact and quantitative fashion based on MCS vertical dust profiles. In Chapter 4.4, I use the scheme developed in Chapter 4.3 to analyze zonal average dust opacity profiles, both as a guide to interpretation of the representation scheme and also as a way of investigating planetary-scale variability in the distribution of dust vertically during these seasons and their impact on the radiative forcing of the atmosphere. In Chapter 4.5, I discuss seasonal and diurnal variability in the vertical dust distribution and describe the vertical heating profile due to dust. In Chapter 4.6, I summarize the results of this study. In Chapter 5, I consider the implications of the characteristic vertical dust distribution observed from the middle of northern spring to the middle of northern summer for dust transport processes.

## 4.2 Data and Basic Analysis

### 4.2.1 Retrieval Characteristics

Atmospheric retrievals from MCS observations provide vertical profiles of pressure,  $p$ , (Pa), temperature,  $T$ , (K), dust opacity, i.e., fractional extinction due to dust per unit height,  $d_z\tau$ , ( $\text{km}^{-1}$ ) at  $463 \text{ cm}^{-1}$ , and water ice opacity ( $\text{km}^{-1}$ ) at  $842 \text{ cm}^{-1}$ . All of the vertical profile quantities except pressure are gridded on pressure coordinates at approximately a factor of five higher resolution than the  $\sim 5 \text{ km}$  vertical resolution of the instrument detector array (and thus the retrievals). The pressure at the surface,  $p_s$ , (Pa) is extrapolated from the pressure retrieval using the hydrostatic equation. *Kleinböhl et al.* [2009] provides both a history of data and retrieval coverage and also a description of the retrieval algorithm and an evaluation of its success under different observational

conditions. For  $d_z\tau > 10^{-5} \text{ km}^{-1}$ , the estimated uncertainty in  $d_z\tau$  is typically  $\sim 5\%$ . The retrievals analyzed here use an advanced version of the retrieval algorithm, which includes a simple scattering approximation in the radiative transfer.

Retrievals from limb observations have an important limitation key to these investigations. The lowest detector used for the retrieval of dust must have a line-of-sight (LOS) opacity less than 2.5 and a contribution of less than 10% from the surface in the detector field of view (FOV). (Note that the airmass factor in the limb is  $\sim 50$ .) The practical effect is that retrieved vertical profiles of dust (with rare exceptions) do not include information from detectors observing limb paths less than  $\sim 8$  km above the surface. Thus, they provide limited information about dust within the lowest scale height of the atmosphere. In some cases, retrieved profiles only use information from detectors observing at higher levels than  $\sim 8$  km above the surface, further limiting information about low-level dust.

A small number of retrievals from late northern summer of MY 28 are generally omitted from this analysis. Between 9 February 2007 and 14 June 2007 ( $L_s=180^\circ$ — $257^\circ$  of MY 28), MCS operated in a mode known as “limb staring” in which the limb was observed at a constant angle relative to the spacecraft. This degraded mode of operation primarily affects the altitude range of the atmosphere observed by the instrument and the calibration of the data. Therefore, retrievals from data collected from this period provide less information about high altitudes in the southern hemisphere and low altitudes near the north pole than retrievals from data collected when the instrument was scanning the limb. In addition, retrievals from limb staring data have greater uncertainties in areas of the atmosphere where radiances are low due to the poor calibration of the instrument in

limb staring mode. Agreement between retrievals from limb staring and limb scanning retrievals (in which the limb is observed at varying angles) are good [Kleinböhl *et al.*, 2009], but the limited vertical range of limb staring retrievals (and hemispheric differences in the vertical range) makes reconstruction of the dust distribution more difficult.

### 4.2.2 Zonal Averaging and Derived Quantities

To avoid biasing of zonal averages by heavier sampling at particular longitudes, the retrievals are separated into “dayside” (9:00—21:00 LST) and “nightside” (21:00—9:00 LST) bins and further binned in 36 ( $5^\circ$  resolution) mean latitudinal bins, 64 ( $5.625^\circ$  resolution) mean longitudinal bins, and  $L_s$  bins at  $5^\circ$  resolution: a resolution comparable to Mars general circulation model grids. Mean latitude and longitude refer to the coordinates at the tangent point observed by the center of the MCS detector array at  $\sim 40$  km above the surface. Since MCS retrievals have relatively broad horizontal weighting functions biased in the direction of the detector array, this latitude and longitude is usually a better indicator of the location of even dust retrieved near the surface than the latitude and longitude at which the limb intersects the surface.

Caution must be exercised when averaging aerosol opacity retrievals. Aerosol opacity is not reported at all in some retrievals for a variety of reasons, such as that there is a high likelihood of misattribution of opacity to one aerosol vs. another, as happens with carbon dioxide ice and dust at the winter pole. See Kleinböhl *et al.* [2009] for further discussion. Retrievals without any reported aerosol opacity are not included in the averages reported here. In all other cases, aerosol opacity is reported at some continuous

subset of pressure levels, for example, each pressure level in a range from 200 to 20 Pa. At pressures higher than 200 Pa, there is not enough information to retrieve aerosol opacity accurately. At pressures lower than 20 Pa, the radiance contributed by the aerosol opacity is comparable to the noise of the radiance measurements. In the averaging process, the unreported aerosol opacity at high pressures is not included, that is, the average of the retrieved aerosol opacity at 200 Pa is the average of all aerosol opacities reported at 200 Pa. But since the unreported opacity on the lower pressure end is unreported because it is so low, the retrieval is altered so that these unreported values have a value of 0 instead. This averaging routine minimizes the effects of a small number of retrievals with measurable aerosol opacity at high altitudes.

The variability in the longitudinal sampling of the zonal averages is depicted in Figures 4.1a and 4.1b. Longitudinal sampling is controlled by a variety of factors, some of which are intrinsic to the data as collected by the instrument, e.g., periods in which data was not collected because the instrument was stowed, and some of which are related to the limitations of the retrieval algorithm, e.g., the exclusion of retrievals with a bad pressure retrieval due to high LOS optical depth in the channels used for pressure retrieval. The absolute breaks in coverage in an  $L_s$  bin are indicated in white. The break at  $L_s=210^\circ$  during MY 28 is a period during which the instrument was stowed.

Figures 4.1a and 4.1b suggest longitudinal sampling by dayside profiles is much poorer than from nightside profiles. In fact, dayside coverage over the equator is practically non-existent. This discrepancy is not well understood but may be due to incorrect representation in the retrieval algorithm of the scattering by tropical water ice clouds of upwelling radiation from the surface.

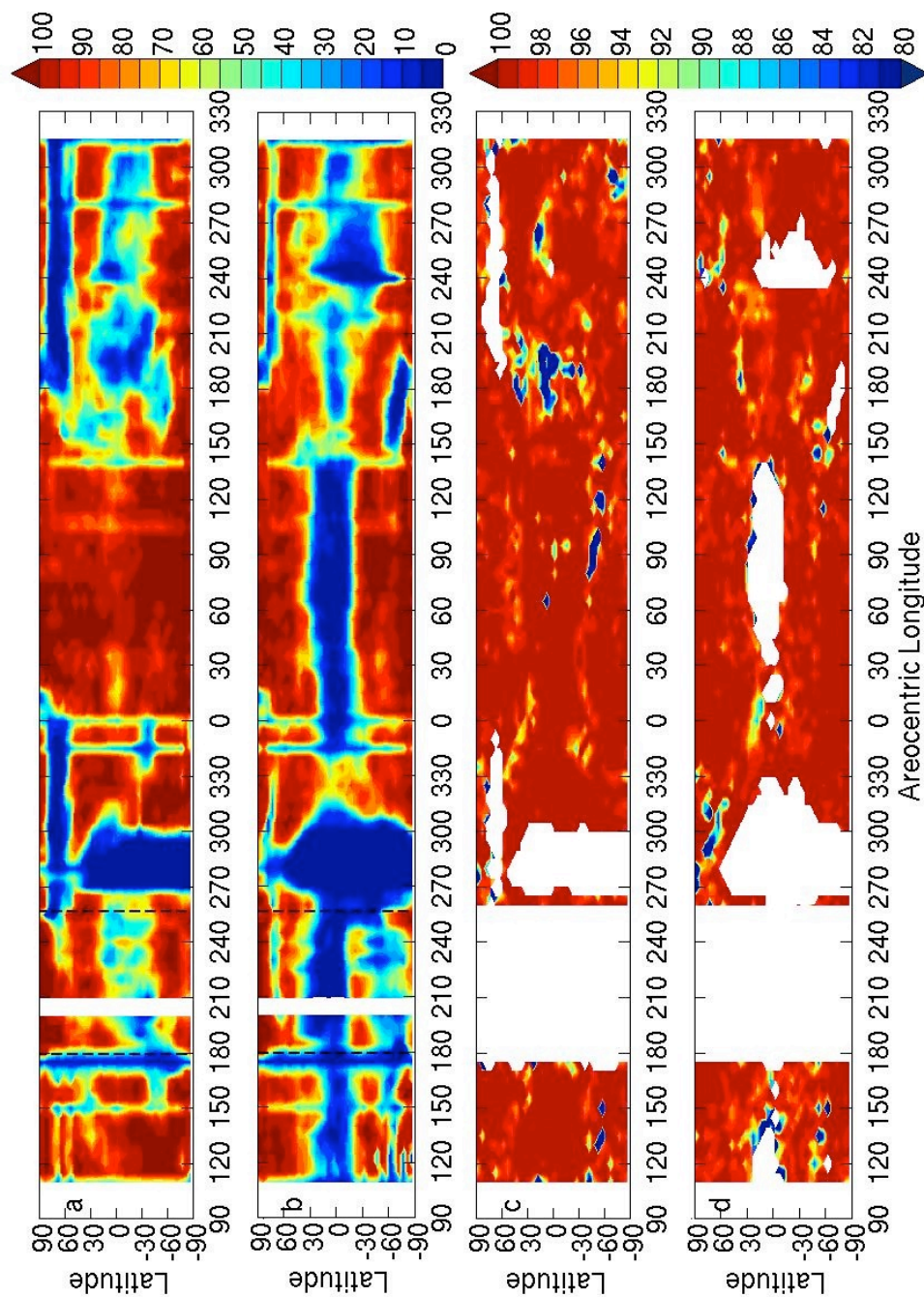


**Figure 4.1.** (a) Percentage of longitudes in the binning scheme described in Chapter 4.2.2 sampled by nightside retrievals vs. latitude and  $L_s$ ; (b) percentage of longitudes in the binning scheme described in Chapter 4.2.2 sampled by dayside retrievals as a function of latitude and  $L_s$ ; (c)  $100 \cdot R^2$  for the empirical fitting scheme described in Chapter 4.3.2 for nightside retrievals as a function of latitude and  $L_s$ ; (d)  $100 \cdot R^2$  for the empirical fitting scheme described in Chapter 4.3.2 for dayside retrievals as a function of latitude and  $L_s$ .

### 4.2.3 A5 Channel Opacity and the Utility of Density

#### Scaled Opacity

For a variety of scientific and engineering applications (including some discussed in this Chapter), opacity in the A5 channel is not a particularly convenient or intuitive quantity to use. However, it is the retrieved quantity related to dust that most immediately follows from MCS observations of radiance. The conversion factor between A5 channel opacity and visible opacity at 600—700 nm is  $\sim 7.3$ . This factor differs from what is reported in *Kleinböhl et al.* [2009], because it accounts for the higher visible/infrared opacity ratio of the smaller dust particles assumed in the new retrieval algorithm [*Clancy et al.*, 2003].

Given some model of the size, shape, and composition of the dust particles, opacity can be converted to three other quantities: volumetric number density,  $N_v$ ; mass number density,  $N_m$ ; and mass mixing ratio,  $q$ . For consistency's sake, I make the same assumption as used in the retrieval algorithm: that the dust is compositionally uniform and made of spherically symmetric particles with a modified gamma size distribution of the form:

$$n(r) \propto r^a \exp(-br^c) \quad (4.1)$$

The parameters used for the dust distribution in the version of the retrieval dataset used here are not the same as in *Kleinböhl et al.* [2009] but have been tuned to minimize misfitting error in the retrieval algorithm.

Following *Taylor et al.* [2007], the opacity as a function of the volumetric number density is:

$$d_z \tau = \int_0^{\infty} Q_{ext} \pi r^2 N_v n(r) dr \quad (4.2)$$

The variables,  $\pi$ ,  $N_v$  and  $Q_{ext}$  can be extracted from the integral, since the latter is only a function of the dust distribution, not of radius, such that:

$$N_v = \frac{d_z \tau}{Q_{ext} \pi \int_0^{\infty} r^2 n(r) dr} \quad (4.3)$$

The value of  $Q_{ext}$  used by the retrieval algorithm is 0.35.  $\pi \int_0^{\infty} r^2 n(r) dr$  in Eq. 4.3 is the average geometric cross-section of the distribution,  $G$ . So Eq. 4.3 becomes:

$$N_v = \frac{d_z \tau}{Q_{ext} G} \quad (4.4)$$

where  $G$  is assumed to be  $1.26 (\mu\text{m})^2$  in the retrieval algorithm. So  $N_v (\text{m}^{-3}) = 2.3 \times 10^9 d_z \tau (\text{km}^{-1})$ . The mass number density,  $N_m$ , then can be obtained by dividing  $N_v$  by the atmospheric density,  $\rho$ .

The mass mixing ratio is obtained similarly. Scaling Eq. 4.3 by  $\rho$ , we obtain the density-scaled opacity:

$$\frac{d_z \tau}{\rho} = \frac{N_v Q_{ext} \pi}{\rho} \int_0^{\infty} r^2 n(r) dr \quad (4.5)$$

We can form an expression for the mass mixing ratio by calculating the ratio between the mass of dust particles in a given volume and the mass of air in the same volume:

$$q = \frac{\rho_D N_v \int_0^{\infty} \frac{4}{3} \pi r^3 n(r) dr}{\rho} \quad (4.6)$$

Eqs. 4.5 and 4.6 can be combined so that:

$$q = \frac{4}{3} \frac{\rho_D}{Q_{ext}} \frac{d_z \tau}{\rho} \frac{\int_0^{\infty} r^3 n(r) dr}{\int_0^{\infty} r^2 n(r) dr} \quad (4.7)$$

The integral ratio above is equal to “the effective radius,”  $r_{eff}$ , which is 1.06  $\mu\text{m}$  for the distribution used by the retrieval algorithm. So:

$$q = \frac{4}{3} \frac{\rho_D}{Q_{ext}} \frac{d_z \tau}{\rho} r_{eff} \quad (4.8)$$

Assuming  $\rho_D = 3000 \text{ kg m}^{-3}$ ,  $q \text{ (ppm)} = 1.2 \times 10^4 d_z \tau / \rho \text{ (m}^2 \text{ kg}^{-1}\text{)}$ .

Since these derivations are model dependent, we only will report  $d_z \tau$  and  $d_z \tau / \rho$ , which can be derived from the retrievals directly. For dust with definite, spatially and temporally invariant distributions of size, shape, and composition, the number density is linearly proportional to  $d_z \tau$ , and the mass mixing ratio is linearly proportional to  $d_z \tau / \rho$ .

If Eq. 4.8 is re-arranged,  $d_z \tau / \rho$  is proportional to the product of  $Q_{ext} / r_{eff}$  and  $q$ . The parameter  $Q_{ext}$  is dependent on the size distribution, so that if there is significant particle size segregation in the atmosphere, variability with size in  $Q_{ext} / r_{eff}$  could result in inferring an apparent enhancement of mass mixing ratio above the surface when no enhancement is actually present. For example, if small dust particles lie over large ones and  $Q_{ext} / r_{eff}$  is significantly larger for small particles, a given mass mixing ratio of small particles will have greater opacity than the same mass mixing ratio of large particles.

Table 4.1 shows the results of Mie scattering simulations of  $Q_{ext}$  for dust size distributions with different  $r_{eff}$  but the same variance as the size distribution used in the retrievals. The variability in the ratio over a reasonable size range for dust is no more

**Table 4.1.** Results of Mie scattering simulations to test the sensitivity of  $Q_{ext}/r_{eff}$  in the MCS A5 channel to particle size

$r_{eff}$ ( $\mu\text{m}$ )	$Q_{ext}/r_{eff}$ ( $\mu\text{m}^{-1}$ )	$Q_{ext}/r_{eff}$ normalized by the value at 1.06 $\mu\text{m}$
0.75001	0.3095	0.970
1.06070	0.3305	1
1.50000	0.3619	1.10
2.12160	0.3956	1.20
2.99930	0.4137	1.25
4.2432	0.3998	1.21
5.99960	0.3524	1.07

than 30%. In addition, the segregation of sub-micron particles over greater than micron-sized particles will produce an apparent depletion of mass mixing ratio in a truly uniformly mixed profile. This analysis, however, does not consider the effect on the retrieval procedure of assuming different particle size distributions.

The rough interchangeability of mass mixing ratio and density scaled opacity is useful for understanding the radiative and dynamical significance of particular vertical profiles of dust. In an optically thin atmosphere (even for non-uniform dust), the quantity  $d_z\tau/\rho$  also is proportional to the unit heating rate per unit mass due to dust at fixed wavelength,  $J$ . Thus, the dust mass mixing ratio (outside of dust storm conditions) is a good proxy for the diabatic heating rate and vice versa.

## **4.3 A New Scheme for Representing Martian Vertical Dust Distributions**

### **4.3.1 Motivation**

*Conrath* [1975] created an idealized profile for representing vertical dust distributions in the martian atmosphere by considering the competing effects of sedimentation and mixing during a decaying global dust storm and modeling the mass mixing ratio of dust in the atmosphere as:

$$q = q_0 \exp[\nu(1 - \sigma^{-1})] \quad (4.9)$$

where  $q_0$  is the mass mixing ratio at the surface,  $\nu$  is the ratio between the characteristic dust diffusion time and the characteristic dust sedimentation time at the surface (the Conrath parameter), and  $\sigma$  is  $\exp(-z/H)$ , where  $z$  is the height and  $H$  is the atmospheric

scale height. In the isothermal approximation of the atmospheric pressure and density profiles generally used by *Conrath* [1975] and in a coordinates system with a small pressure at the top of the domain ( $p_{top}$ ), this definition of  $\sigma$  is approximately equal to the definition of  $\sigma$  used in GCMs for the coordinates of the vertical computational grid:

$$\sigma = \frac{P - P_{top}}{P_s - P_{top}} \quad (4.10)$$

When used in a GCM, e.g., *Forget et al.* [1999], a pseudo- $\sigma$ ,  $\tilde{\sigma} = p/p_0$ , is often substituted for  $\sigma$  in Eq. 4.9, where  $p_0$  is a reference pressure, e.g., 700 Pa in *Forget et al.* [1999], below which  $q$  is taken to be  $q_0$ .

*Forget et al.* [1999] modified this scheme of *Conrath* [1975] using analyses of Mariner and Viking data by *Anderson and Leovy* [1978] and *Jaquin et al.* [1986] to account for the seasonal variability in the height of observable dust in the atmosphere:

$$q = q_0 \exp[\nu(1 - \tilde{\sigma}^{-l})] \quad (4.11)$$

where  $l$  is equal to the ratio between a reference height,  $Z_0$  and the maximum height of observed dust,  $z_{max}$ , which is treated as a function of latitude and areocentric longitude ( $L_s$ ).

The column opacity,  $\tau$ , is the integral of Eqs. 4.9 or 4.11 with height from the top of the atmosphere to the level of interest, provided they are multiplied by  $\rho_0\sigma$  or  $\tilde{\rho}_0\tilde{\sigma}$  to recover  $d_z\tau$ , and then multiplied by  $dz = Hd\sigma/\sigma$  or  $Hd\tilde{\sigma}/\tilde{\sigma}$  to permit integration on the  $\sigma$  coordinates to obtain optical depth. But as first described by *Conrath* [1975], the resulting optical depths involve exponential integrals, which are computationally expensive. Thus, the GCM described by *Forget et al.* [1999] actually computes optical depth as:

$$\tau = \tau_0 \tilde{\sigma} \exp[\nu(1 - \tilde{\sigma}^{-1})] \quad (4.12)$$

which is obtained using a similar procedure to the exact integration by assuming that the exponential function in Eq. 4.12 is a constant (a suitable approximation for  $\nu=0.007 \ll 1$ ) and incorporating  $H$ ,  $\rho_0$ , and  $q_0$  into a reference optical depth,  $\tau_0$ .

The vertical dust distribution reconstructed from MCS dust profiles suggest there is a need for an alternative scheme to those of *Conrath* [1975] and *Forget et al.* [1999] to quantify vertical variation in the mass mixing ratio of dust, Figure 4.2 shows a zonal average of nightside retrievals from  $L_s=87.5^\circ$  to  $92.5^\circ$  (hereafter called  $L_s=90^\circ$  for shorthand) of two quantities: (1) the density scaled opacity (filled color contours) calculated from the retrieved temperature, pressure, and dust opacity; (2) the numerically evaluated height derivative of Eq. 4.12, i.e., the dust opacity (red contours), calculated from the observed pressure and temperature scaled as for (1). The values of  $\tau_0$  used to calculate (2) are those used in the Mars Year 24 scenario of the Mars Climate Database [Lewis et al., 1999; Montmessin et al., 2004] scaled by a factor of 3.6 to account for the assumed visible/infrared MCS dust opacity ratio and the visible/9  $\mu\text{m}$  opacity ratio used in *Forget et al.* [1999]. The key feature of this figure is the contrast between the nearly constant density-scaled opacity bubble between 60—400 Pa produced by the modified Conrath scheme of *Forget et al.* [1999] and the greater and more vertically narrow maximum in density-scaled opacity at  $\sim 60$  Pa observed in the MCS retrievals near the equator and both poles. (The slight enhancement in the Mars Year 24 scenario distribution at  $\sim 60$  Pa is an artifact of a spurious thermal inversion often retrieved in the tropical lower atmosphere in this season and represents an 8% enhancement above the near-surface dust density scaled opacity.) Note that the mean density scaled opacity at the

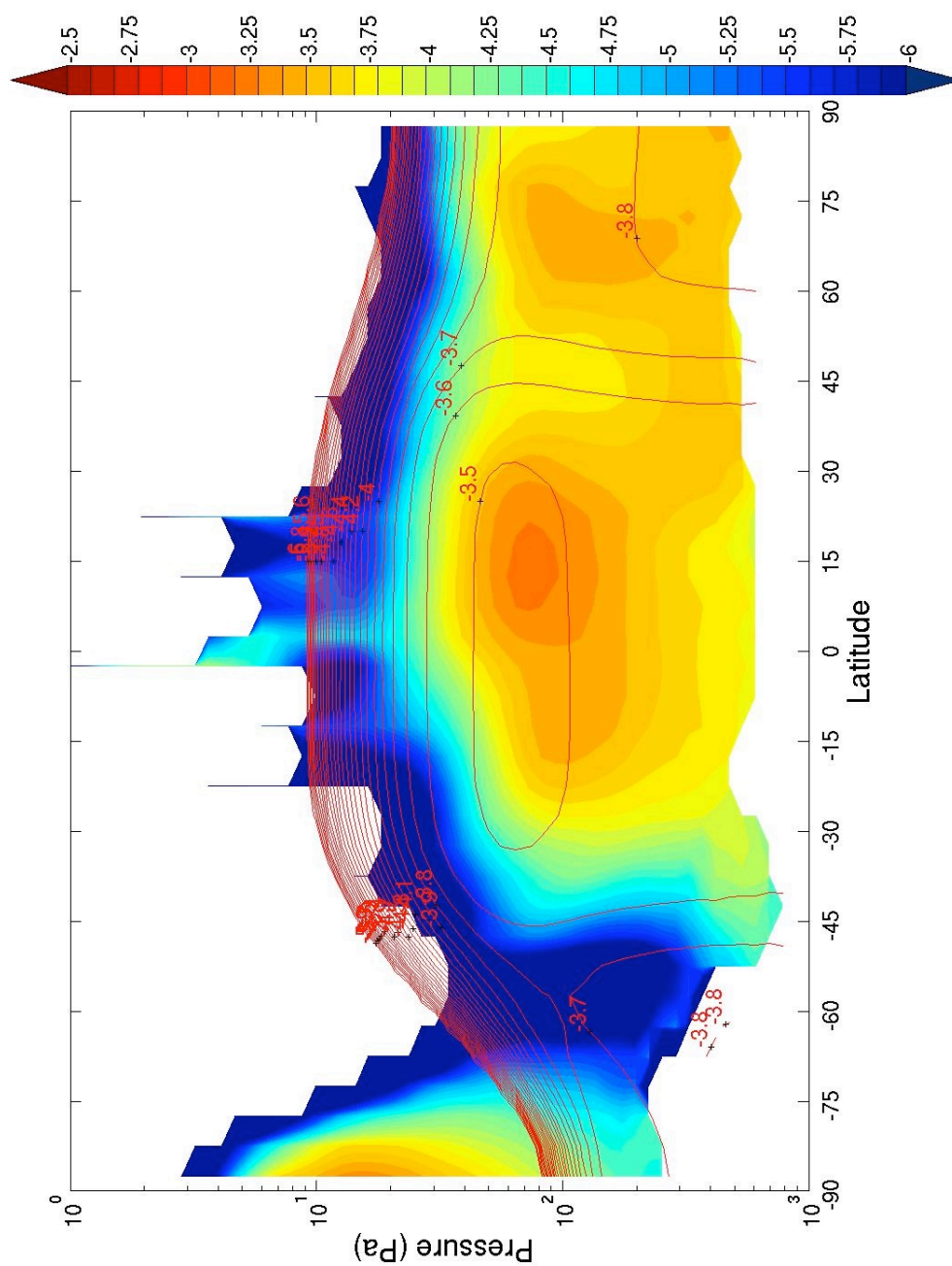


**Figure 4.2.**  $\text{Log}_{10}$  of zonal average dust density scaled opacity ( $\text{m}^2 \text{kg}^{-1}$ ) interpolated onto pressure coordinates for nightside retrievals,  $L_s=90^\circ$ , MY 28: (colors) from MCS retrievals; (labeled red contours) based on the Mars Year 24 MGS dust scenario in the Mars Climate Database with MCS retrieval pressure and temperature information. Contours are every 0.1 log units. White space below the colors indicates no data. White space above the colors and the darkest blue indicates density scaled opacity below  $10^{-6} \text{m}^2 \text{kg}^{-1}$ .

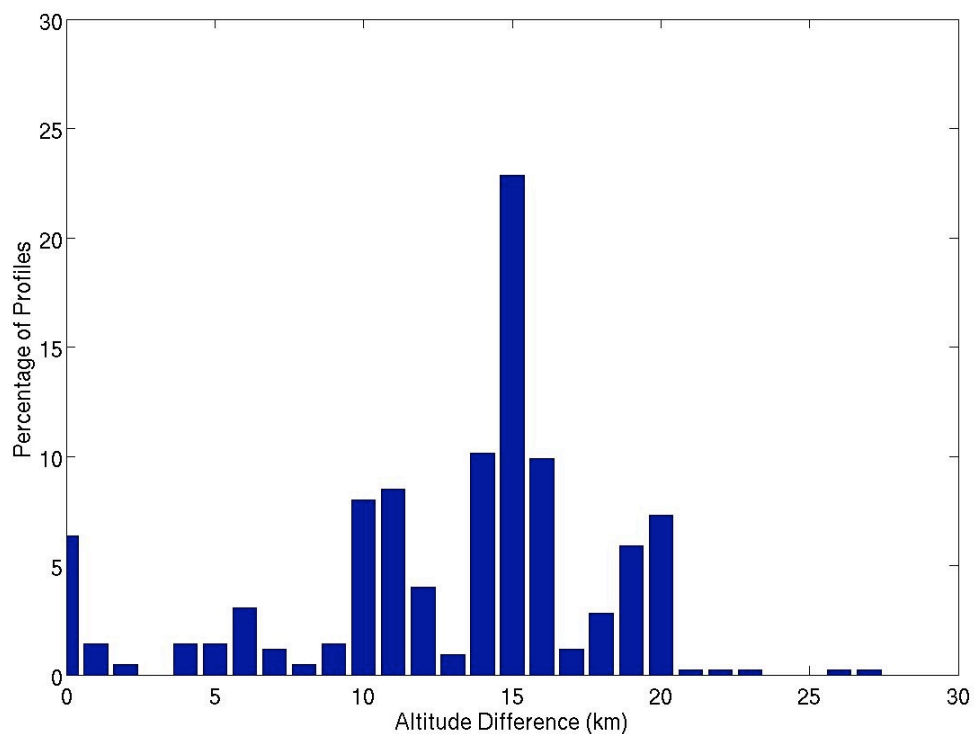


**Figure 4.3.** Histogram of the difference between the lowest altitude (relative to the Mars Orbiter Laser Altimeter areoid) at which dust opacity was reported and the altitude at which the highest dust density scaled opacity was calculated in each individual retrieval (424 total) from  $20^{\circ}$  to  $25^{\circ}$  N,  $L_s=90^{\circ}$  of MY 29, nightside.

highest pressure levels with reported opacity is a factor of four smaller than the density scaled opacity maximum. A region of dust-clear air near 60° S is also apparent.

The appearance of the “high altitude tropical dust maximum” in the zonal average of dust density scaled opacity is indicative of the large number of individual retrieved profiles with maxima in dust density scaled opacity well above the lower end of the retrieved profile. Figure 4.3 shows the distribution of the difference in altitude (calculated from the pointing of the instrument) between the lowest level of the profile at which dust is reported and the level at which the maximum dust density scaled opacity occurs for all individual retrievals from 20° to 25° N, MY 29 on the nightside (within the high altitude tropical dust maximum in Figure 4.2). Around 90% of retrieved profiles have a maximum in dust density scaled opacity at least 5 km above the lower end of the retrieved profile. The typical difference is ~15 km. Thus, the high altitude tropical maximum is a maximum in dust density scaled opacity normally within the vertical range of individual MCS retrieved profiles.

A Conrath profile will not fit the high altitude tropical dust maximum or a similar feature. Let us consider one of the zonally averaged density scaled opacity profiles depicted in Figure 4.2 (Figure 4.4a) and re-write Eq. 4.9 to obtain a  $\sigma$ -varying Conrath parameter:

$$\nu(\sigma) = \frac{\ln \frac{q}{q_0}}{1 - \sigma^{-1}} \quad (4.13)$$

Figure 4.4b shows the result of inverting the profile in Figure 4.4a with Eq. 4.13 by assuming a value of  $q_0$  extrapolated from the highest  $\sigma$  level with density scaled opacity information, that is, the value of  $q$  nearest the surface and thus the one that might

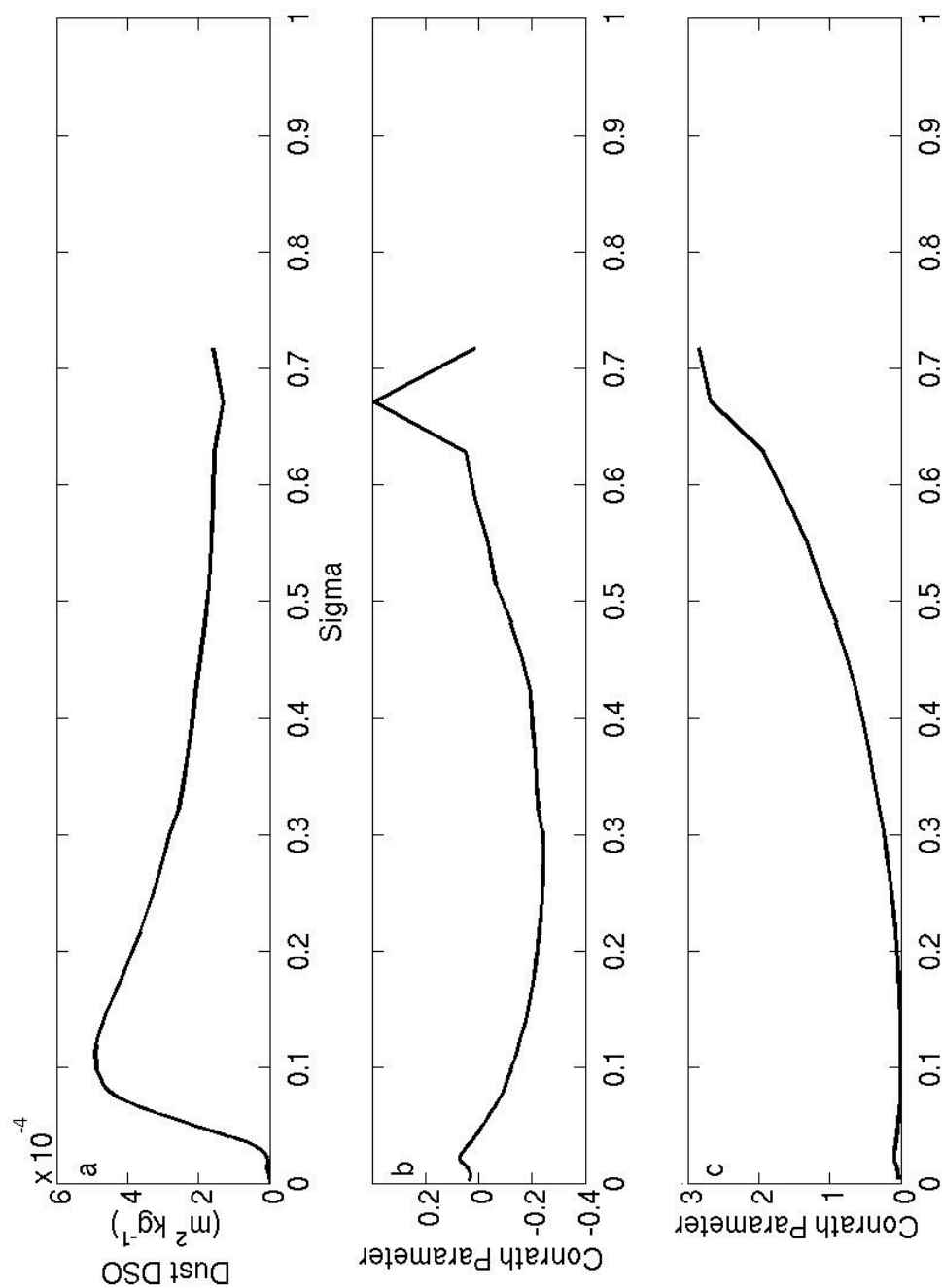


**Figure 4.4.** (a) Zonal average of the density scaled opacity ( $\text{m}^2 \text{kg}^{-1}$ ) interpolated onto  $\sigma$  coordinates for nightside retrievals,  $L_s=90$ , MY 28,  $10^\circ\text{--}15^\circ \text{N}$ ; (b) inferred Conrath parameter,  $v(\sigma)$  for the profile in (a), assuming  $q_0=1.61 \times 10^{-4} \text{ m}^2 \text{kg}^{-1}$ ; (c) inferred Conrath parameter,  $v(\sigma)$  for the profile in (a), assuming  $q_0=4.92 \times 10^{-4} \text{ m}^2 \text{kg}^{-1}$ .

be characteristic of  $q$  in a relict well-mixed convective boundary layer. This inversion results in negative values of the Conrath parameter over a broad range of  $\sigma$ . Most fundamentally, the Conrath parameter is the ratio between the rates of sedimentation and vertical atmospheric diffusion. The model of *Conrath* [1975] accounts for the decrease of the rate of sedimentation with height due to lower atmospheric density, so variability in the Conrath parameter with respect to a vertical coordinate should be interpreted as variability in the vertical atmospheric diffusivity with that vertical coordinate. Therefore, the negative Conrath parameter region in Figure 4.4b is presumably one with negative vertical atmospheric diffusivity, where dust diffuses (in a purely mathematical sense) from regions of lower concentration to those of higher concentration.

Figure 4.4c shows the result of inverting the profile in Figure 4.4a with Eq. 4.13 by assuming a value of  $q_0$  equivalent to the density scaled opacity maximum in the profile. In this case, the Conrath parameter increases toward higher  $\sigma$  (or lower altitude), which could be interpreted to mean that vertical diffusion weakens closer to the surface of Mars, precisely the region of the atmosphere in which vertical diffusion should be most vigorous due to turbulent interactions between the atmosphere and the surface. Thus, the presence of a maximum in mass mixing ratio except at the surface is inconsistent with the assumptions underlying the Conrath profile and motivates an alternative representation scheme for the vertical variation of dust mass mixing ratio in Mars's atmosphere.

### 4.3.2 Design of the Scheme

This new scheme models opacity retrievals from Mars Climate Sounder as a function of  $\sigma$  in order to represent two principal features observed by inspection of the zonal average density scaled opacity profiles: (1) the decay in density scaled opacity with height and (2) the high altitude maxima in dust density scaled opacity observed significantly above the surface of the tropics and sometimes near the poles. The scheme is empirical and not based on any particular physical model of vertical dust transport. The choice of  $\sigma$  as a vertical coordinate allows easier use of the scheme in GCMs, is quickly adaptable to pressure-gridded MCS retrieved profiles (which also have a retrieved surface pressure), and also was based on the hypothesis that since the ultimate source of dust is the surface, the vertical distribution of dust should be a function of height above the surface. For simplicity, I, like *Conrath* [1975], make use of the isothermal approximation of the variation of the atmospheric density with height.

Opacity was assumed *a priori* to be of the form

$$d_z \tau(\sigma) = d_z \tau_1 \sigma f(\sigma) \quad (4.14)$$

where  $d_z \tau_1$  is a kind of extrapolated surface opacity, not the opacity in the lowest truly retrieved layer. Eq. 4.14 permits the shape of the density scaled opacity profile (the approximate mass mixing ratio) to be modeled as  $f(\sigma)$  and also permits fairly direct integration of  $f(\sigma)$  to obtain optical depth under a simplification described below.

To derive a suitable form of  $f(\sigma)$ , zonally averaged profiles of opacity in  $5^\circ L_s$  bins at from nightside and dayside profiles were interpolated onto a logarithmic  $\sigma$ -grid (105 evenly spaced points from  $10^{-3}$  to 1) and then scaled by  $\sigma$ . The shapes of these

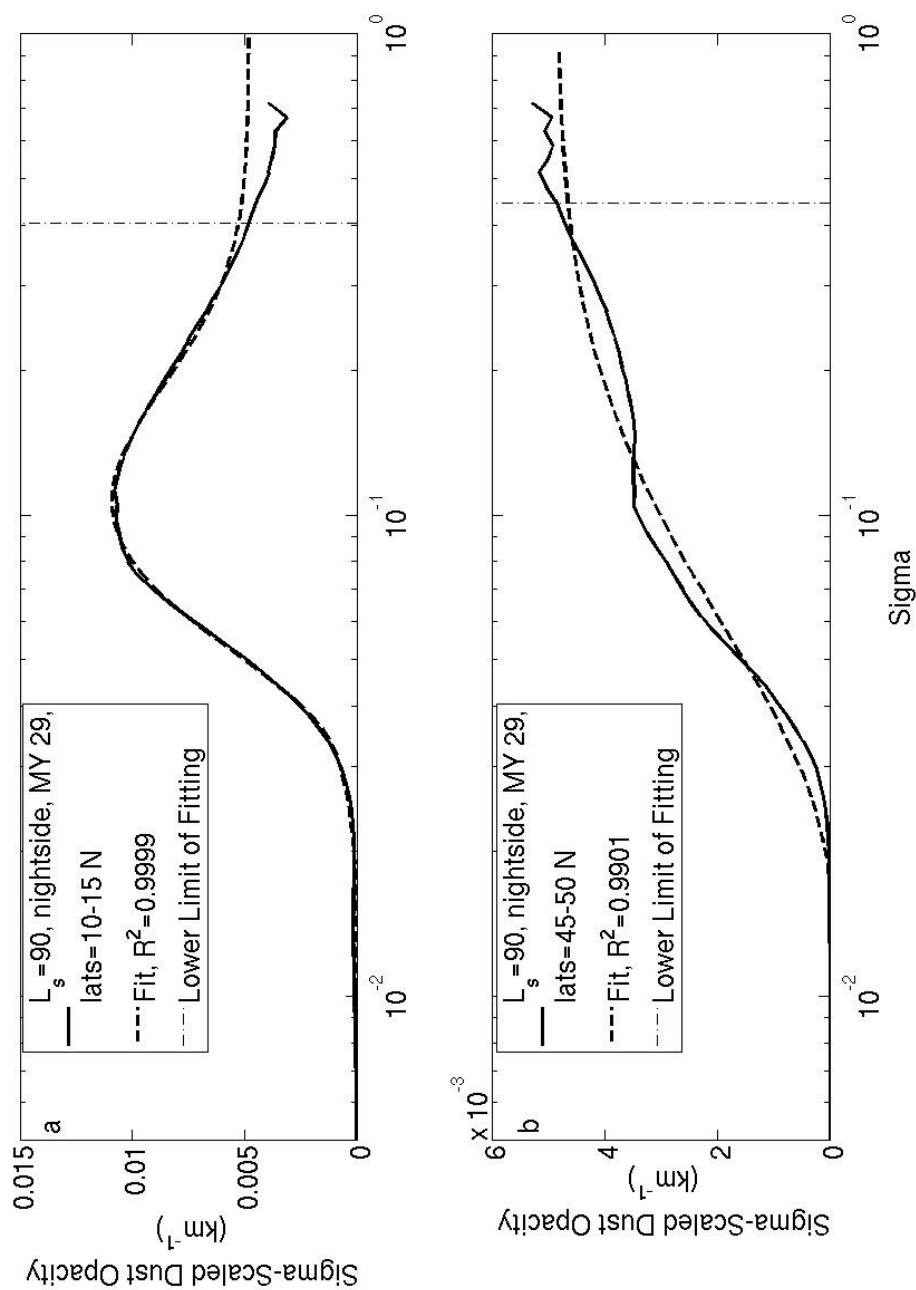


**Figure 4.5.** Demonstration examples for the fitting scheme which show the zonal average of opacity interpolated onto  $\sigma$  coordinates and scaled by  $\sigma$  (solid line) and the resultant fits (dashed line). (a) Tropical profile used in Figure 4.4 that has a global maximum “pulse” ( $d_z \tau_I = 4.8 \times 10^{-3} \text{ km}^{-1}$ ,  $B = 1.2855$ ,  $\sigma_0 = 0.0312$ ,  $\sigma_I = 0.1030$ ,  $m_0 = 0.6343$ ,  $m_I = 0.8452$ ); (b) northern mid-latitude profile with a weak local maximum that the implemented scheme does not consider significant enough to fit ( $d_z \tau_I = 4.9 \times 10^{-3} \text{ km}^{-1}$ ,  $\sigma_0 = 0.016$ ,  $m_0 = 1.8803$ ). The dot-dashed lines show the lower limits of where the zonal average profiles are fit.

scaled profiles fall into two qualitative categories: “perturbed” (Figure 4.5a) and “unperturbed” (Figure 4.5b) profiles (solid lines). Unperturbed profiles have an approximately monotonic fall off from a roughly uniform profile at a value assumed to be approximately equal to  $d_z \tau_1$  (probably indicative of a relict or true well-mixed convective boundary layer) to near zero scaled opacity at the top of the grid. Perturbed profiles have a significant global (or sometimes local) maximum in scaled opacity at some  $\sigma < 1$ . Even the example “unperturbed” profile in Figure 4.5b appears to be slightly perturbed at  $\sigma=0.1$ . Inspection suggested that a good  $f(\sigma)$  for unperturbed profiles was:

$$f(\sigma) = \Xi(\sigma - \sigma_0) \left\{ 1 - \exp \left[ \frac{-(\sigma - \sigma_0)^2}{m^2} \right] \right\} \quad (4.15)$$

where  $\Xi$  is the Heaviside function (the notation prevents confusion with the scale height,  $H$ ) and  $\sigma_0$  is a parameter that effectively sets the top of significant dust in the profile whereas  $m$  is a measure of the rapidity of its decay.

Eq. 4.15 produces a poor fit (not shown) to the solid curve in Figure 4.5a due to the perturbation in the scaled opacity centered at  $\sigma \approx 0.08$ . This perturbation can be fit by an additional Gaussian unmultiplied by the Heaviside function, yielding:

$$f(\sigma) = \Xi(\sigma - \sigma_0) \left\{ 1 - \exp \left[ \frac{-(\sigma - \sigma_0)^2}{m_0^2} \right] \right\} + B \exp \left[ \frac{-(\sigma - \sigma_1)^2}{m_1^2} \right] \quad (4.16)$$

where  $B$  is the amplitude of the perturbation,  $m_1$  is a parameter that governs its width, and  $m_0$  is the same as  $m$  in Eq. 4.16.

Some zonal average profiles and some individual retrieved dust profiles have multiple perturbations. In that case, fitting with multiple Gaussians could be appropriate. Ideally, there would be some discrete boundary between unperturbed and perturbed

profiles (and thus for an unperturbed profile, fitting using Eq. 4.16 would result in  $B=0$ ), but, of course, this situation rarely occurs in practice due to the contributions to zonal averages from mixtures of unperturbed and perturbed profiles with perturbations at multiple levels. In addition, overinterpolation and overfitting of the profiles often allows Gaussians to be fit to minor perturbations that may not be statistically significant. An ad hoc solution to this problem will be discussed in Chapter 4.3.3.

If we substitute Eq. 4.16 into Eq. 4.14 and integrate in the same way as the Conrath schemes, we can obtain an optical depth function:

$$\tau(\sigma) = Hd_z \tau_1 \left\{ \Xi(\sigma - \sigma_0) \left[ \sigma - \frac{m_0}{2} \sqrt{\pi} \operatorname{erf} \left( \frac{\sigma_0 - \sigma}{m_0} \right) \right] + \frac{Bm_1 \sqrt{\pi}}{2} \left[ \operatorname{erf} \left( \frac{\sigma_1}{m_1} \right) - \operatorname{erf} \left( \frac{\sigma_1 - \sigma}{m_1} \right) \right] \right\} \quad (4.17)$$

where erf signifies the error function. While this form is not necessarily practical for GCM use, it is useful for reconciling total optical depths from nadir observations with idealized or true vertical profile information more easily obtained from off-nadir measurements.

Eq. 4.16, however, is inappropriate for fitting MCS data. Consider the logarithmic  $\sigma$  scale used to plot the profiles in Figures 4.5a-b. On this scale, the perturbation appears to be a standard symmetric Gaussian. On a linear  $\sigma$  scale, however, the peak is skewed toward higher values of  $\sigma$ . The result is that the fitting routine tries to fit the peak by effectively introducing opacity at very high altitudes, which will introduce a radiatively-dynamically important artifact if used in future to develop a prescribed dust scheme. The problem is actually quite intuitive. The vertical weighting functions of MCS retrievals should be roughly symmetric in height (and thus in  $\ln \sigma$ ), so features in them should be

symmetric and best fit by symmetric functions in the same types of coordinates system. Thus, we revise Eq. 4.16:

$$f(\sigma) = \Xi(\ln\sigma - \ln\sigma_0) \left\{ 1 - \exp\left[\frac{-(\ln\sigma - \ln\sigma_0)^2}{m_0^2}\right] \right\} + B \exp\left[\frac{-(\ln\sigma - \ln\sigma_1)^2}{m_1^2}\right] \quad (4.18)$$

where the fit is of parameters  $\ln(\sigma_0)$  etc., not of  $\sigma_0$  directly, and  $m_0$  and  $m_1$  are setting Gaussian widths in a different coordinates system than in Eq. 4.16.

Eq. 4.18, however, is not as readily analytically integrable as Eq. 4.16. One very approximate approach would be to fit a profile with Eq. 4.18 and to use Eq. 4.16 in applications (such as prescribed dust schemes) by converting  $\ln\sigma_0$  to  $\sigma_0$ . However,  $m_0$  and  $m_1$  cannot be transformed between coordinate systems in the same way. The conversion factor can be derived by denoting  $m$ -parameters in Eq. 4.16 by hats and equating one of the analogous Gaussians in Eqs. 4.16 and 4.18 as follows:

$$\exp\left[\frac{-(\ln\sigma - \ln\sigma_0)^2}{m_0^2}\right] = \exp\left[\frac{-(\sigma - \sigma_0)^2}{\hat{m}_0^2}\right] \quad (4.19)$$

This reduces to:

$$m_0 \frac{\sigma - \sigma_0}{\ln\sigma - \ln\sigma_0} = \hat{m}_0 \quad (4.20)$$

which implies that the transformation is itself a function of  $\sigma$ . But we will not require that the scaling be exact everywhere and will decide to seek the scaling where it is most important, that is, at  $\sigma = \sigma_0$ . We then convert Eq. 4.20 to a limit:

$$m_0 \left( \lim_{\sigma \rightarrow \sigma_0} \frac{\sigma - \sigma_0}{\ln\sigma - \ln\sigma_0} \right) = \hat{m}_0 \quad (4.21)$$

The limit can be evaluated using L'Hôpital's rule such that:

$$m_0\sigma_0 = \hat{m} \quad (4.22)$$

providing the desired transformation between  $m$ -parameters in the different coordinates systems.

### 4.3.3 Fitting Profiles Using the Scheme

In some cases, Eq. 4.18 may overfit the data. The nominal resolution of the MCS limb retrievals is somewhat greater than the resolution of measurements with which they were made. The procedure that uses Eq. 4.18 begins with an individual opacity retrieval, which: (1) is interpolated onto a logarithmically spaced  $\sigma$  grid (an operation that results in additional oversampling of the data); (2) is averaged with similarly interpolated retrievals in the same latitude-longitude bin on a  $5^\circ$  (latitude) by  $5.625^\circ$  (longitude) bin; (3) is zonally averaged with all bins with data; (4) is scaled by the logarithmically-spaced  $\sigma$  grid; (5) which is finally fit on the logarithmically-spaced  $\sigma$  grid. The averaging process (as in the profile in Figure 4.4a) can introduce a variety of small noisy features that could be fit with individual Gaussians nearly *ad infinitum*.

This potential oversampling/overfitting catastrophe may be avoided in two ways. First, interpretations that are dependent on differences much smaller than the “detector width” of  $\sim 5$  km should be rejected. Thus, using the fact that the scale height,  $H$ , of the martian atmosphere is  $\sim 10$  km and the difference between two  $\sigma$  levels,  $\sigma_x$  and  $\sigma_y$ , in height is  $\sim H \ln(\sigma_x/\sigma_y)$ , differences much less than  $\sim 65\%$  between a  $\sigma$ -level parameter are probably not statistically significant. Second, the major overfitting risk in the scheme is to use Eq. 4.18 and so fit some statistically insignificant feature in the scaled opacity profile, when Eq. 4.15 (if transformed to  $\ln \sigma$  coordinates) is more suitable. Fitting the

zonal average profiles just with Eq. 4.18 produced likely fitting artifacts such as small  $B$  with  $m \approx 100$ . We were able to reduce the occurrence of these artifacts by fitting a profile separately with Eq. 4.18 and the logarithmic version of Eq. 4.15 and then performed an F-ratio test using the residual sum of squares from each fit ( $RSS_{15,18}$ ), where  $F$  is defined as:

$$F = \frac{\frac{RSS_{15} - RSS_{18}}{RSS_{15}}}{\frac{p_{18} - p_{15}}{n - p_{18}}} \quad (4.23)$$

and where  $p_{15}$  and  $p_{18}$  are the number of free parameters in Eqs. 4.15 and 4.18,  $p_{18}=5$  and  $p_{15}=2$  respectively, and  $n$  is the number of degrees of freedom in the data. Ideally, this ratio tests the null hypothesis that Eq. 4.15 is a better fit to the data than Eq. 4.18 by comparison with an F distribution with parameters  $p_{18}-p_{15}$  and  $n-p_{18}$ . Practically, such a test can be implemented by assuming that  $RSS$  will scale linearly with increasing  $n_{\text{fit}}$ , so that an F-ratio test is possible for these overinterpolated profiles using an estimate of the intrinsic  $n$  of the data. Ignoring the averaging and interpolation,  $n$  should be approximately equal to 5 for an individual dust opacity retrieval, since  $\sim 5$  detectors in the A5 channel of MCS are used to retrieve dust. However, A5 radiances are dependent on the temperature profile as well, so the  $\sim 8$  detectors in channels A1, A2, and A3 observe the same part of the limb as the A5 detectors to retrieve temperature, thereby providing some implicit constraint on dust. For the fits presented in this Chapter,  $n$  is conservatively assumed to be 10. The critical value of the F-ratio for the 95% confidence interval for  $n=10$  is 5.4095, which was used to determine whether a profile should use Eq. 4.15 or

Eq. 4.18. The use of this test explains why the small local maximum in Figure 4.5b is not fit.

The diagnosis of  $d_z\tau_l$  presented an additional problem. In Figure 4.5a, it appears that the  $\sigma$ -scaled opacity decreases toward the surface at the lower altitude end of the data. In other zonal average profiles, the opposite trend is seen. If a zonally and vertically averaged  $H$  is derived from the available temperature data between 100 and 1000 Pa (or the lowest available pressure level failing any data at pressures greater than 100 Pa), many of these features appear to occur at heights of significantly less than 8 km above the surface. Thus, these features may originate from uncertainties in the extrapolated surface pressure or instances with extremely low LOS opacity near the surface. Thus, we diagnose  $d_z\tau_l$  by determining the  $\sigma$ -scaled opacity that would correspond to the  $\sigma$  level corresponding to 8 km above the surface, or failing that, at a  $\sigma$  level 35% less than that. If there is no data at even this  $\sigma$  level, the fitting scheme is not used. These flexible criteria allow the fitting scheme to be used in almost all areas with available retrievals in northern spring and summer, particularly in late northern summer near the north pole, where low level water ice clouds normally limit the vertical range of retrievals to 12-13 km. Outside of this region,  $d_z\tau_l$  is almost always a diagnosis of the 8 km  $\sigma$ -scaled opacity. Due to this method of diagnosis, the perturbation features either can be accentuated or diminished relative to the lower region of assumed uniform mixing. In addition, the fitting is only done on the domain between the  $\sigma$  level of diagnosis and the top of the domain at  $\sigma=10^{-3}$ .

The fitting scheme was implemented using standard Matlab non-linear fitting algorithms. These algorithms seek to minimize the unfit variance of the fit. If these algorithms are used without guessing initial parameters, the fitting routine often either

finds a local minimum in unfit variance that is a qualitatively and quantitatively poor fit or fails to converge on a solution entirely. To minimize these problems, the fitting scheme guessed initial parameters by mimicking the strategy I would have used to fit the curve by trial and error. For example,  $\sigma_0$  should mark where  $\sigma$ -scaled opacity is “cut off” by the Heaviside function and is clearly  $\sim 0.02$  in the example profile in Figure 4.5b, so an initial guess of  $\sigma_0$  is based on locating where the mass mixing ratio falls below a certain ratio to the extrapolated mass mixing ratio at the surface. As another example,  $B$  and  $\sigma_1$  are guessed from the amplitude and location of the highest amplitude local maximum in  $\sigma$ -scaled opacity. We cannot prove definitely that the global minimum in unfit variance is found in all cases, only that the fitting scheme in most cases produces solutions that agree well with the solution obtained by trial and error in the hundreds of cases considered during the process of designing the fitting scheme.

The fitting scheme was implemented on all zonal average bins with available retrievals, both nightside and dayside. Figures 4.5a-b show example fits that represent the profiles well but illustrate that  $R^2$  is somewhat inflated, since a large part of the domain fit in logarithmic  $\sigma$  space often has limited dust opacity. Only the results for bins in northern spring and summer with available limb-scanning retrievals will be shown. The  $R^2$  for the fits is normally very good ( $>0.9$ ) in northern spring and summer (Figures 4.1c and 4.1d).

The exceptions are generally pathological. The poor fit indicated in Figure 4.1c at around  $L_s=65^\circ$  of MY 29, for instance, is due to the zonal average profile containing two local maxima in dust density scaled opacity of similar magnitude that are widely

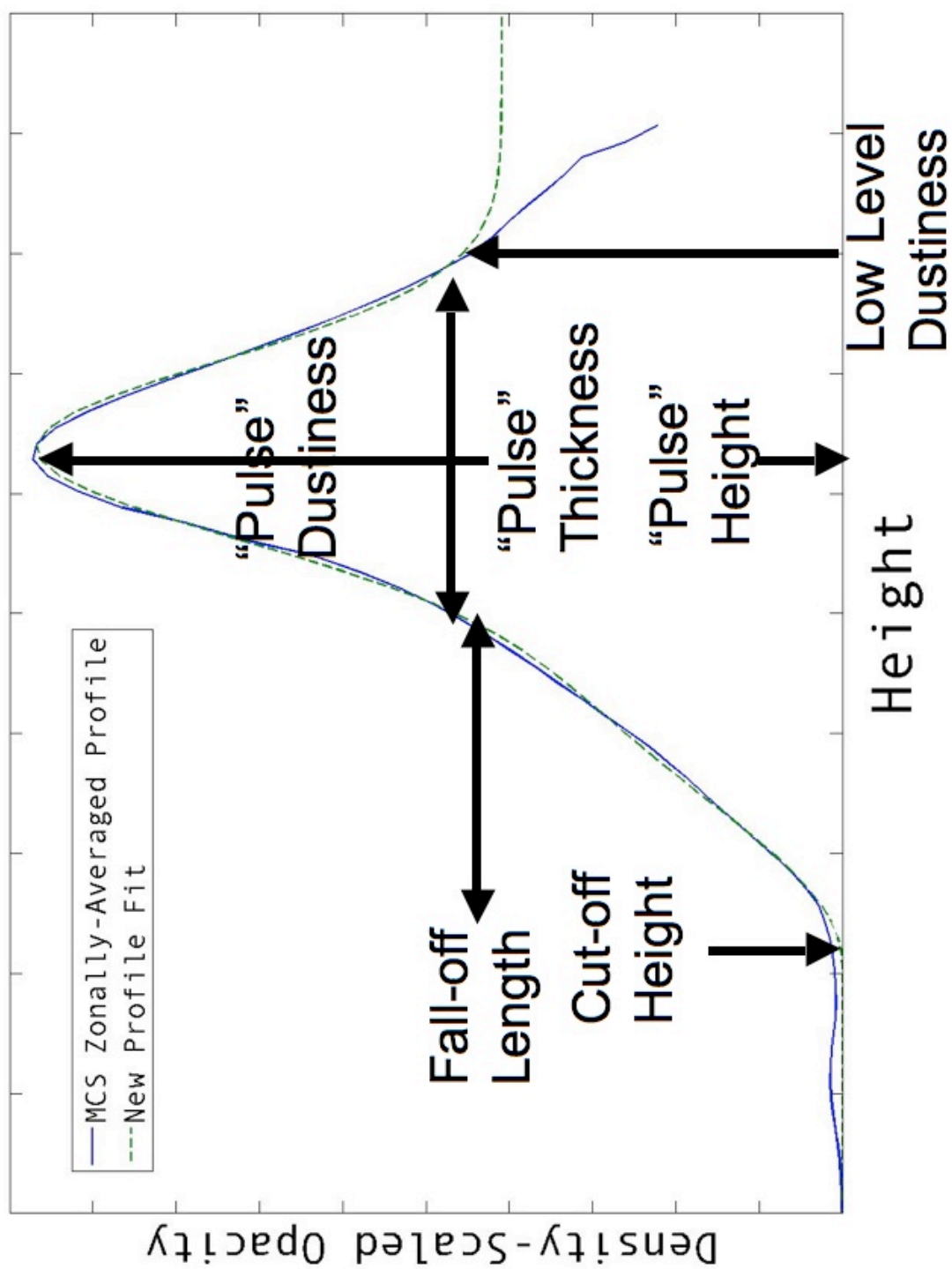


**Figure 4.6.** Schematic of how fitting scheme can be used to derive six parameters that can represent how the vertical distribution of dust changes within Mars's atmosphere.

separated in altitude. The local maximum at high altitude ( $\sim 50$  km) is a relatively rare feature of the zonal average profiles at this latitude and season.

#### 4.3.4 Deriving More Intuitive Parameters from the Fitting Scheme

While the parameters of Eq. 4.18 are structured conveniently for curve fitting, the connection between their variability and variability in the distribution of mass mixing ratio with height is not always intuitive. For example, in the dust clear region,  $B$  is often very high, possibly because dust is not being lifted at the surface but intrudes from lower latitudes at relatively high altitude. While  $B$  is proportional to the magnitude of the maximum in dust mass mixing ratio sufficiently above  $\sim 8$  km from the surface, we cannot use  $B$  to track the latitudinal and seasonal variability in this high altitude dust maxima seen in Figure 4.2 in the tropics and near the south pole. Yet the parameters in Eq. 4.18 may be combined with one another,  $H$ , and  $\rho_0$  (the estimated atmospheric density at the surface) to derive six parameters whose seasonal and latitudinal variability does indicate important changes in the vertical distribution of dust. (The atmospheric density at the surface is estimated in each individual retrieval from  $p_s$  and a temperature derived from extrapolation of constant potential temperature from the highest pressure level at which temperature is reported to the surface). A schematic representation of these parameters is given in Figure 4.6.

First, a “low level dustiness” (LLD), the characteristic density scaled opacity/mass mixing ratio in the vertical range of MCS observations nearest to the

surface, can be defined, which may be in some cases be representative of the mass mixing ratio of dust in the boundary layer [*Hinson et al.*, 2008]:

$$LLD = \frac{d_z \tau_1}{\rho_0} \quad (4.24)$$

Second, Eq. 4.24 is weighted by  $B$  to obtain a characteristic density scaled opacity corresponding to the dust mass mixing ratio in the principal local maximum or global maximum in the profile, the “perturbation” or “pulse dustiness,” PD:

$$PD = B \frac{d_z \tau_1}{\rho_0} \quad (4.25)$$

Note that since the fall off from constant mass mixing ratio generally occurs above this maximum, the true local or global maximum in mass mixing ratio usually is proportional to LLD+PD.

Third, the altitudes above the surface at which the peak of the “pulse” occurs or above which the dust mass mixing ratio cuts off to effectively zero, “the pulse height”, PH, and the cut off height, CH can be estimated as:

$$\begin{aligned} CH &= -H \ln \sigma_0 \\ PH &= -H \ln \sigma_1 \end{aligned} \quad (4.26a-b)$$

Finally, the characteristic length scale of decay of density scaled opacity from LLD to 0 or the characteristic length scale of the “pulse,” the “pulse thickness” (PT) and the “cutoff length” (CL) can be estimated:

$$\begin{aligned} CL &= m_0 H \\ PT &= m_1 H \end{aligned} \quad (4.27a-b)$$

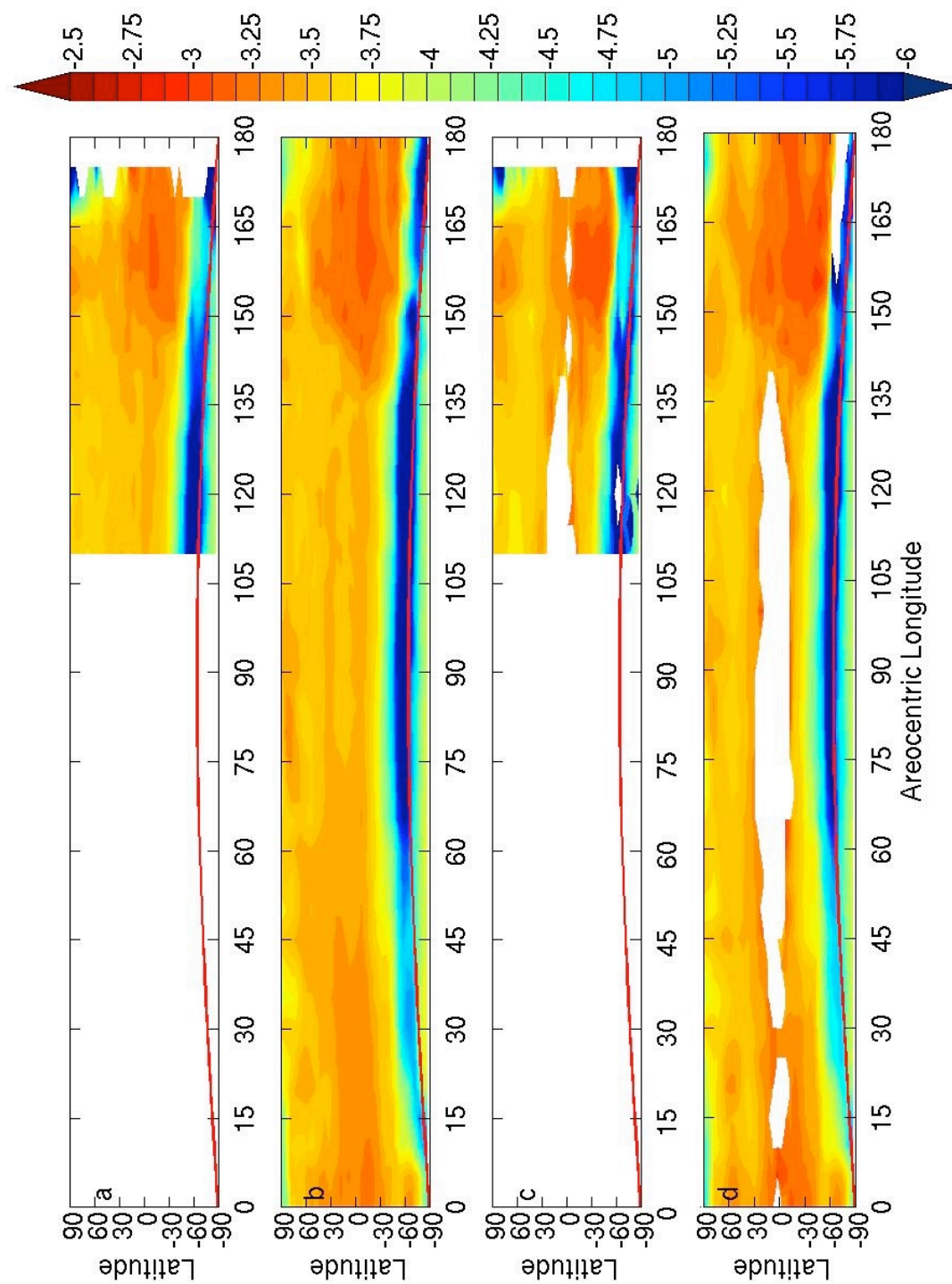


**Figure 4.7.** Latitudinal and seasonal variability in  $\log_{10}(\text{LLD})$ , ( $\text{m}^2 \text{kg}^{-1}$ ) during northern spring and summer. The red line marks the northern edge of southern polar night: (a) MY 28, nightside; (b) MY 29, nightside; (c) MY 28, dayside; (d) MY 29, dayside. White space is missing data. The deepest blue represents  $\text{LLD} < 10^{-6} \text{m}^2 \text{kg}^{-1}$  or effectively dust free areas.

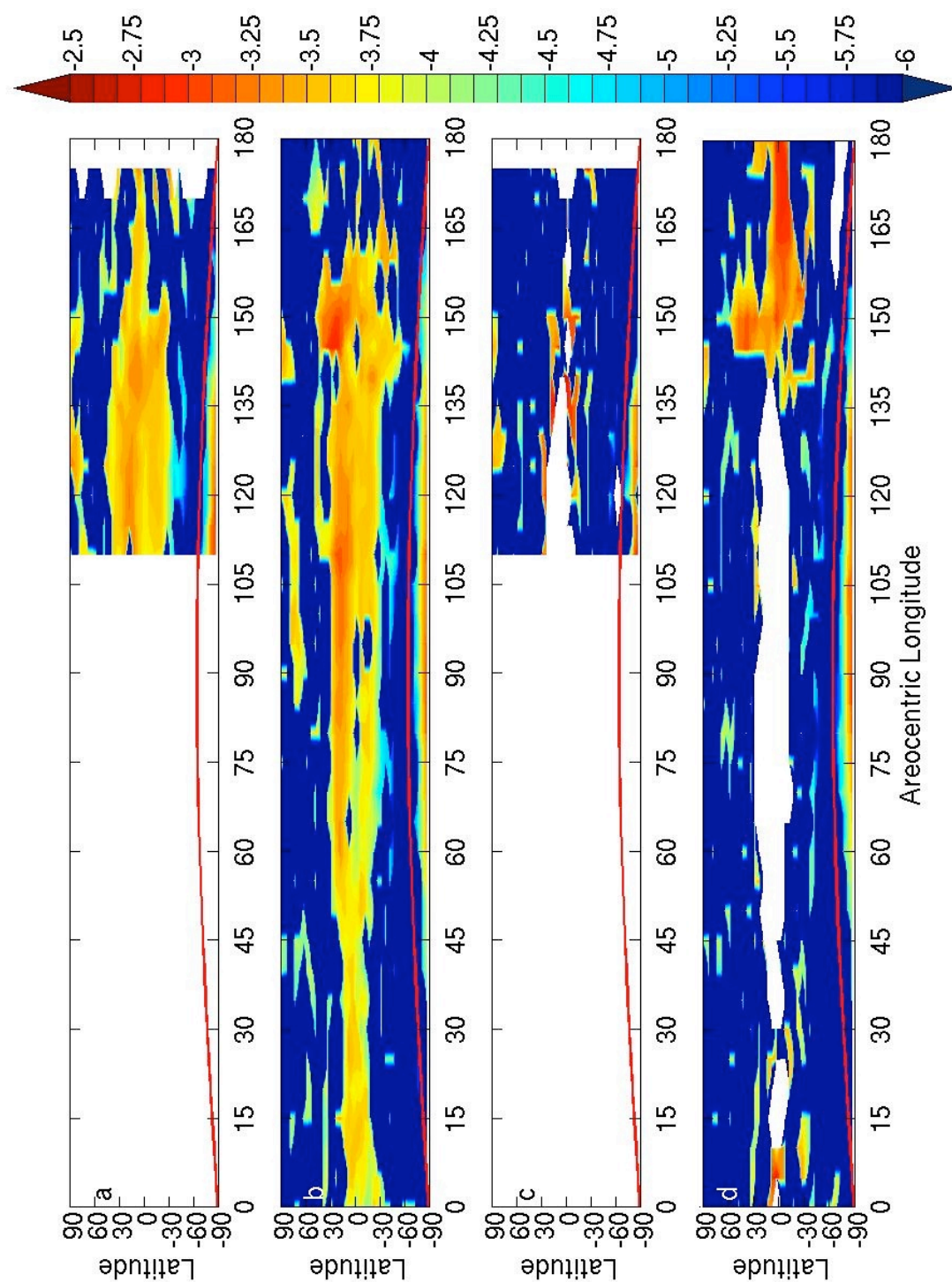


**Figure 4.8.** Latitudinal and seasonal variability in  $\log_{10}(\text{PD})$ , ( $\text{m}^2 \text{kg}^{-1}$ ) during northern spring and summer. The red line marks the northern edge of southern polar night. (a) MY 28, nightside; (b) MY 29, nightside; (c) MY 28, dayside; (d) MY 29, dayside. White space is missing data. The deepest blue represents  $\text{PD} < 10^{-6} \text{m}^2 \text{kg}^{-1}$ .

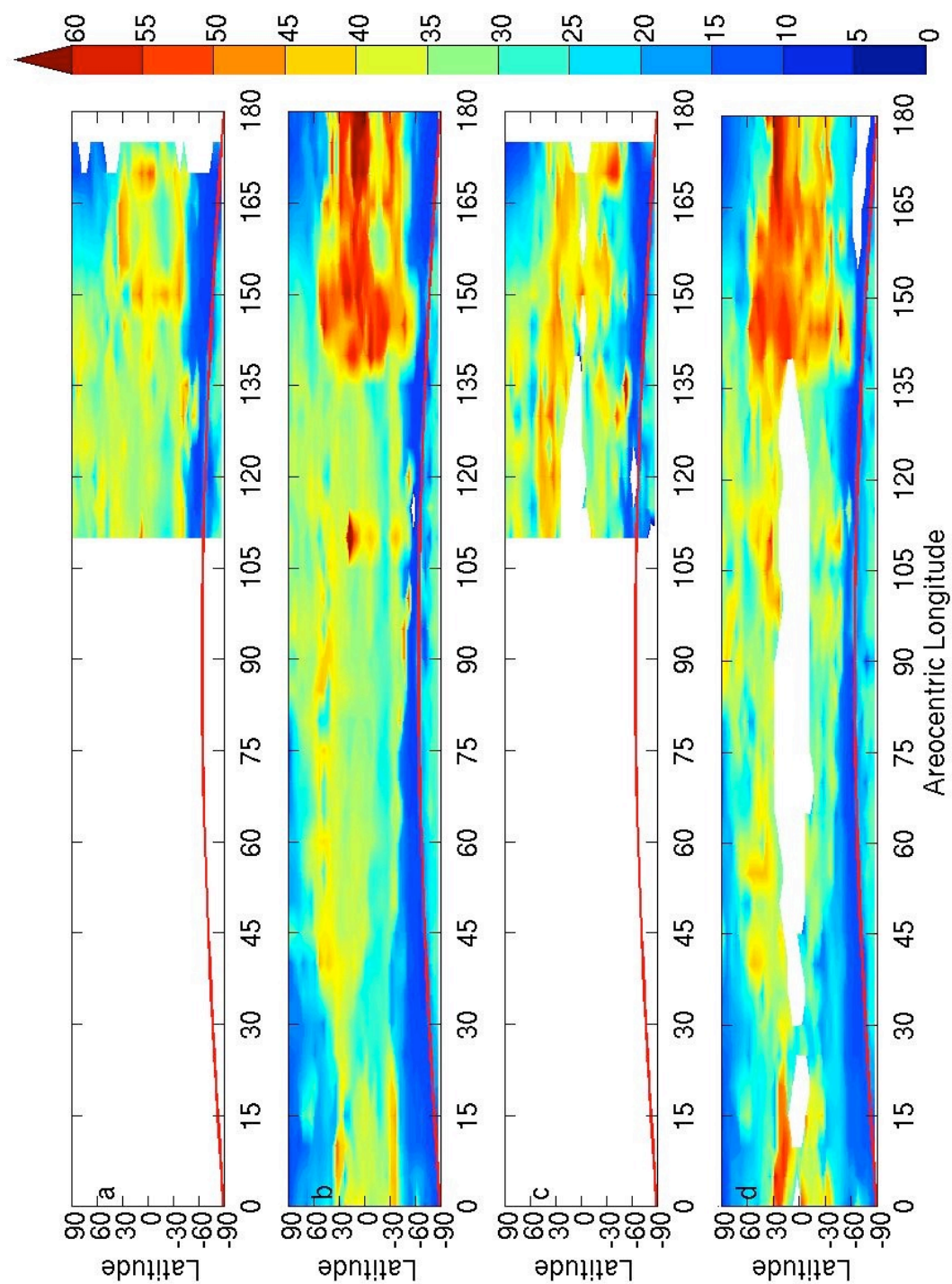


**Figure 4.9.** Latitudinal and seasonal variability in CH (m) during northern spring and summer. (a) MY 28, nightside; (b) MY 29, nightside; (c) MY 28, dayside; (d) MY 29, dayside. The red line marks the northern edge of southern polar night.

## 4.4 Results

Figures 4.7a-d show the seasonal and latitudinal variability in LLD. LLD is  $\sim O(10^{-4} \text{ m}^2 \text{ kg}^{-1})$  throughout the tropics and the northern hemisphere. LLD is significantly lower near the north pole at the beginning of spring and the end of summer in MY 29. LLD is effectively zero  $\sim 15^\circ$  north of the northern edge of southern polar night, a limit which bounds an effective “dust clear” region. Within polar night, LLD increases in the direction of the south pole to values intermediate between the “dust clear region” and the dustier regions to the north of it. Seasonally, northern extratropical LLD is relatively constant, while tropical LLD is higher in early spring and even higher in late summer than in the intervening season as the “dust clear” region shrinks and much higher values of LLD are observed in the southern extratropics. LLD is higher in the northern tropics and mid-latitudes during late summer in MY 29 than in MY 28.

Figures 4.8a-d show the seasonal and latitudinal variability in PD. The contrast between LLD and PD is considerable. In most cases, high values of PD are restricted to the tropics, though PD is also high near the southern pole and at some times in early summer near the northern pole. Significant PD is restricted to very near the equator until  $L_s=35^\circ$  and then is of greater magnitude in the northern tropics than the southern tropics until late summer. PD in the tropics during late summer is generally higher in MY 29 than in MY 28.

Figures 4.9a-d show seasonal and latitudinal variability in CH. CH is less than 10 km throughout the dust-clear region. It is also very low near the north pole in early northern spring and late northern spring, indeed for a longer period than LLD is relatively low in that region at similar times of year. Through most of northern spring and summer

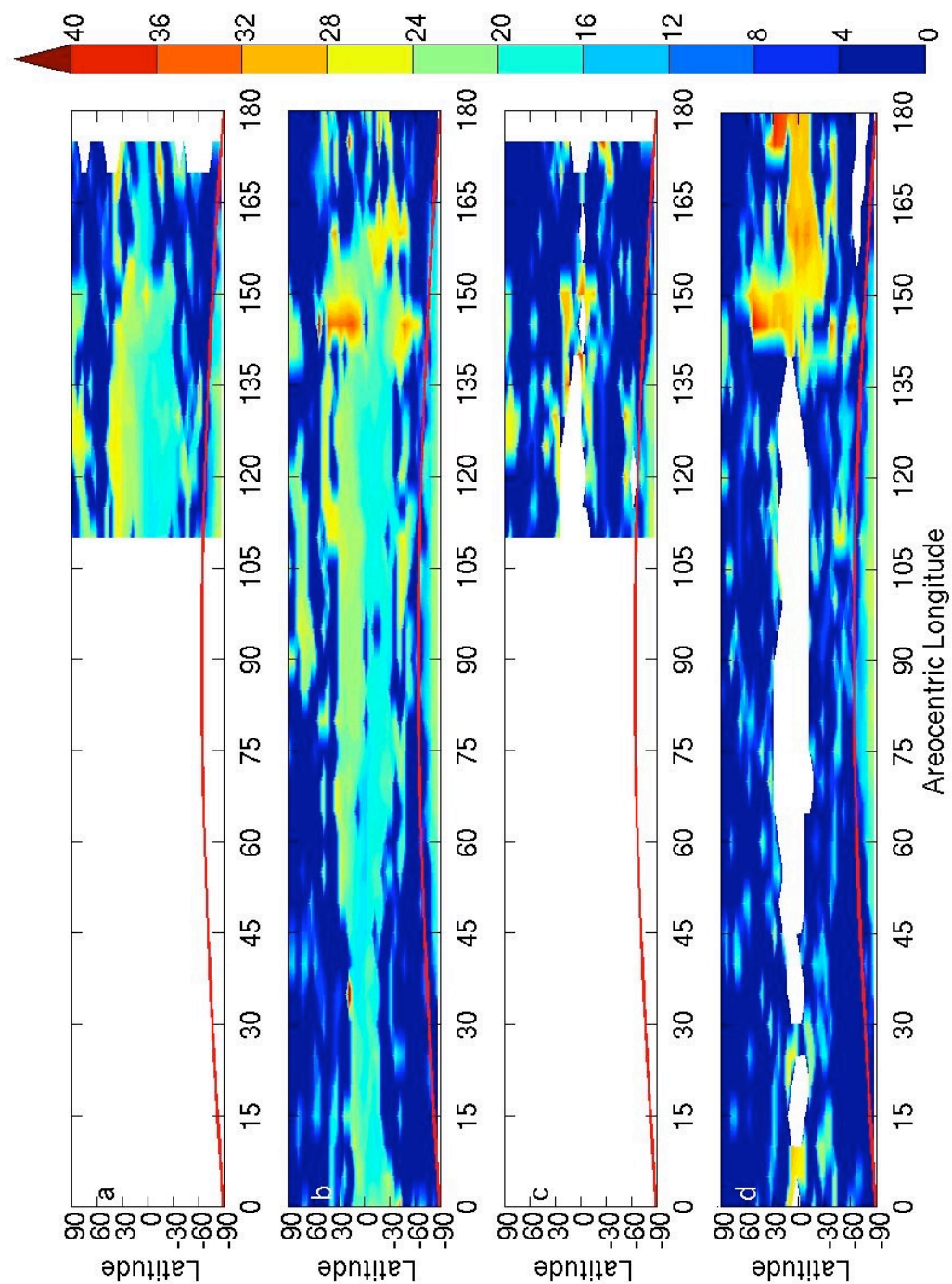


**Figure 4.10.** Latitudinal and seasonal variability in PH (m) during northern spring and summer. (a) MY 28, nightside; (b) MY 29, nightside; (c) MY 28, dayside; (d) MY 29, dayside. The red line marks the northern edge of southern polar night.

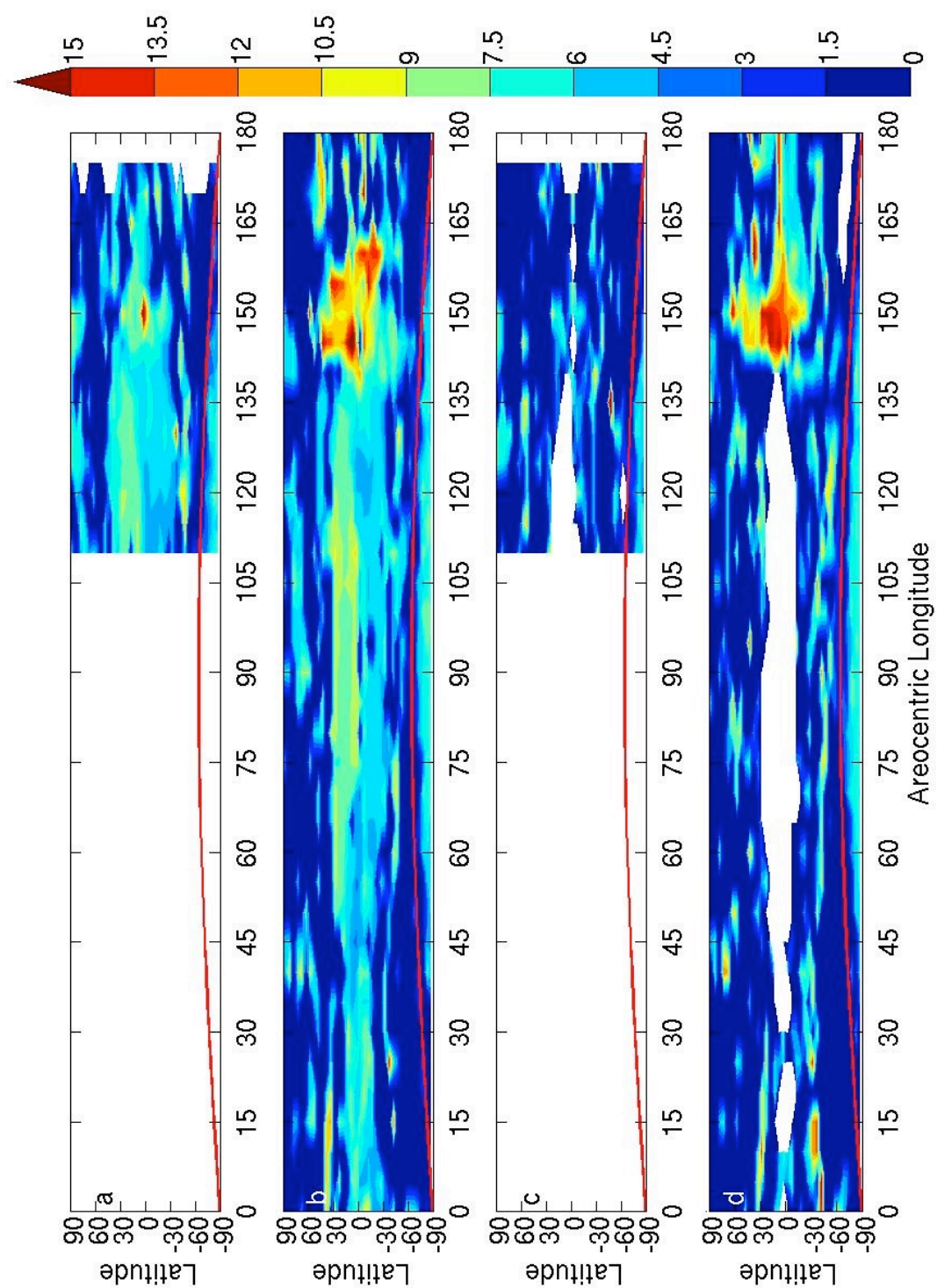


**Figure 4.11.** Latitudinal and seasonal variability in PT (m) during northern spring and summer. (a) MY 28, nightside; (b) MY 29, nightside; (c) MY 28, dayside; (d) MY 29, dayside. The red line marks the northern edge of southern polar night.

over the rest of the planet, CH is  $\sim 20$ — $30$  km. At about  $L_s=150^\circ$  in MY 28, CH in the tropics increases briefly to  $40$ — $45$  km. A little earlier in MY 29 ( $L_s=140^\circ$ ), CH also increases to values as high as  $60$  km. This increase is far more latitudinally broad than in MY 28 and is much longer in duration, lasting at least the end of northern summer. Figures 4.10a-d show seasonal and latitudinal variability in PH. The principal feature of interest is that PH is higher in the northern tropics and slightly further north ( $\sim 20$ — $25$  km) than in the southern extratropics ( $\sim 15$  km). PH of the north and south polar pulses is  $\sim 20$ — $25$  km as well. In the late summer, however, PH differs significantly between MY 28 and MY 29, decreasing from values earlier in the summer in MY 28 but increasing to  $\sim 30$ — $35$  km in dayside profiles in MY 29 after  $L_s=140^\circ$ . Since a pulse at  $\sim 10$  km is a feature effectively irresolvable from low level dustiness, tropical values of PH indicate that the pulse is practically non-existent in the southern tropics during late summer of MY 28. However, the pulse is quite resolvable from low level dustiness through most of the spring and summer, especially in the northern tropics.

Figures 4.11a-d show seasonal and latitudinal variability in PT. The apparent correlation between PH and PT is striking. Higher pulses appear to be thicker pulses. The quantitative thickness could be interpreted in terms of the full width at half maximum of the pulse, which should be  $\sim 1.66$  PT. From this calculation, the high altitude dust maximum in the northern tropics is normally  $12$ — $15$  km ( $2$ — $3$  MCS detectors) thick and is about half of that thickness in the southern tropics. The north polar and south polar maxima also are at least a detector thick by this measure. PT in the tropics increases during late summer of MY 29 to  $12$ — $15$  km. A similar increase is not seen during MY 28.

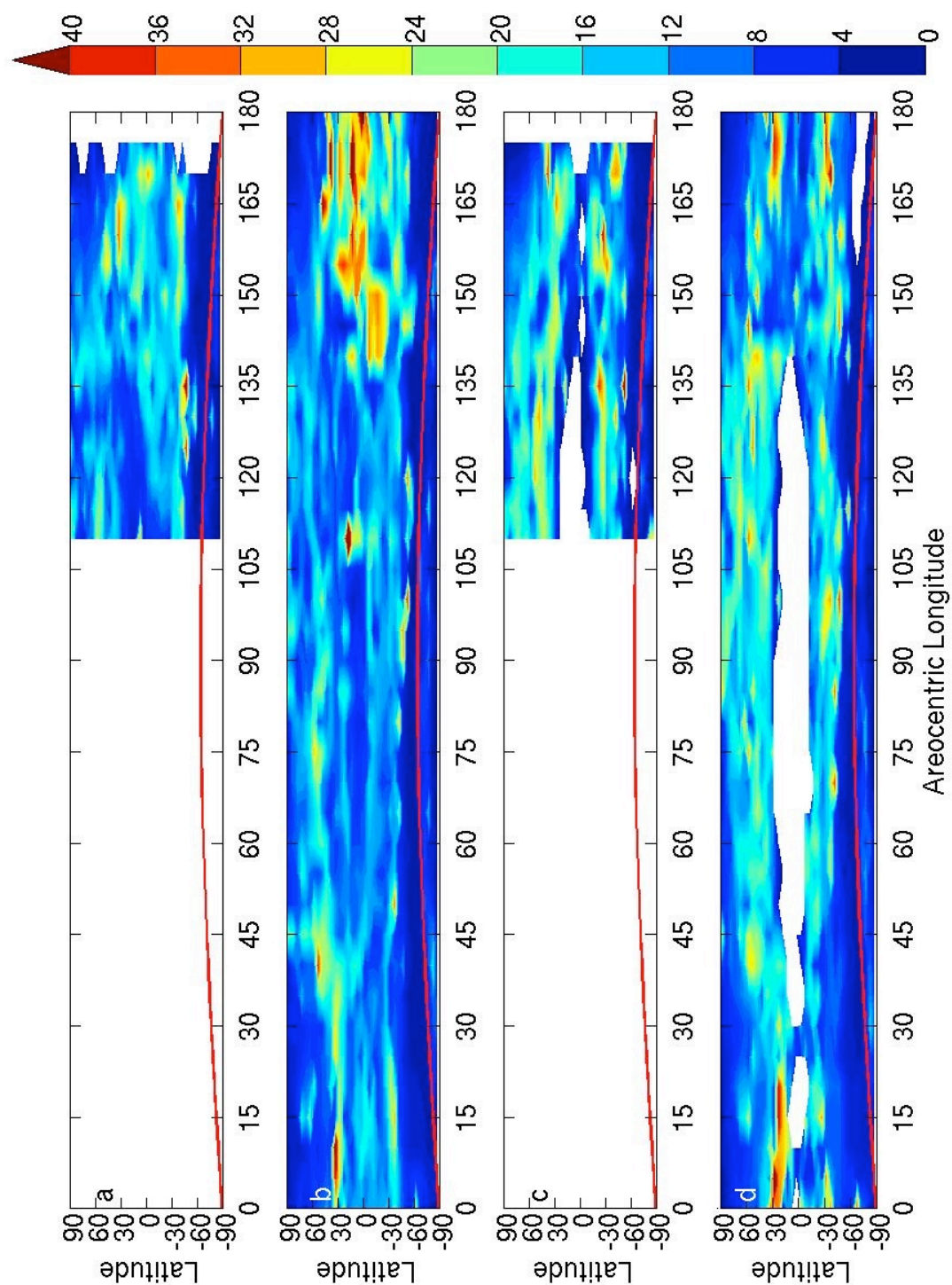


**Figure 4.12.** Latitudinal and seasonal variability in CL (m) during northern spring and summer. (a) MY 28, nightside; (b) MY 29, nightside; (c) MY 28, dayside; (d) MY 29, dayside. The red line marks the northern edge of southern polar night.

Figures 4.12a-d show seasonal and latitudinal variability in CL. This parameter appears to be somewhat noisier than the others with less clear coherent behavior in various latitudinal bands or seasons. The most notable feature is the relatively low tropical values of CL between  $L_s=40^\circ$  and  $140^\circ$  in MY 29 and  $L_s=110^\circ$  and  $155^\circ$  in MY 28, which indicate that tropical dust falls to zero very quickly above the high altitude dust maximum before changes in the tropical vertical dust distribution during late northern summer. CL also generally appears to be higher on the dayside than the nightside.

## 4.5 Discussion

### 4.5.1 The Tropical Dust Distribution

From  $L_s=110^\circ$  to  $160^\circ$  of MY 28 and from  $L_s=45^\circ$  to  $140^\circ$  of MY 29, the tropical dust distribution has a well-defined character. The lower end of MCS's vertical range is clearer of dust than any other time of year (Figures 4.7a-b). At about 25 km above the surface of the northern tropics, dust concentrations are enriched by a factor of two to four relative to the lower end of MCS's range. A generally weaker enrichment is seen in the southern tropics at  $\sim 15$  km above the surface. (Figures 4.8a-b and 4.10a-b). Therefore, the high altitude tropical dust maximum seen in Figure 4.2 and its greater northern magnitude and intensity are persistent features of the planetary vertical dust distribution for roughly a quarter of the martian year. Also notable is that the dust generally penetrates to no higher than 10 km above the high altitude tropical dust maximum (Figures 4.9a-b). This sharp cutoff above the maximum is particularly evident around the

northern summer solstice at the equator (Figure 4.12b), where CL falls below 5000 m. One possible explanation for this sharp cutoff could be the scavenging of the top of the dust haze by water ice condensation. The diurnal variability in CL then may be due to changes in altitude of water ice condensation, which are suspected to be tidally modulated [Lee *et al.*, 2009].

The relative stability of the tropical dust distribution during mid to late spring and early summer makes the changes in the dust distribution at these latitudes at the end of the period all the more striking. In MY 28, the alteration in the dust distribution is relatively gradual: the primary change that can be seen before the period of limb staring is an erosion of the high altitude tropical dust maximum in the southern tropics and mid-latitudes as LLD decreases and a significant pulse no longer can be fit (Figures 4.7a and 4.8a). In addition, PH lowers and the northern extent of the high altitude tropical maximum shrinks (Figure 4.10a), but LLD primarily increases south of the equator. CH increases somewhat at  $L_s=150^\circ$  but only by  $\sim 10$  km (Figure 4.9a). In MY 29, the change is both greater in magnitude and considerably more abrupt. LLD and PD increase suddenly throughout the tropics and into the northern and southern mid-latitudes (Figures 4.7b and 4.7d; Figures 4.8b and 4.8d). In many cases, LLD is greater than PD.

These differences in the seasonal evolution and character in late summer of the dust distribution between MY 28 and MY 29 are likely due to greater “early season” tropical dust storm activity [Malin *et al.*, 2008; Smith, 2009] observed by MARCI and THEMIS, which may most strikingly manifest itself in an aspect of the distribution not as easily observed by these instruments: the depth of penetration of dust. Dustier conditions near the surface also could explain the earlier and greater degradation in longitudinal

sampling and higher values of LLD in the northern tropics and mid-latitudes during this season (Figures 4.1a-b; Figures 4.8a-d) in MY 29. (Note that in late summer of MY 28, MCS was experiencing some technical issues, which resulted in data collection gaps, so the sampling contrast due to retrieval success between MY 29 and MY 28 is not as readily captured by Figures 4.1a-b as it could be).

The results in Chapter 4.4 do not show whether the high altitude tropical dust maximum is present on the dayside as well as the nightside. Retrievals on the dayside near the equator around northern summer solstice are difficult due to the high LOS opacity due to water ice in some MCS channels. Successful retrievals that meet quality control standards in this region and season generally do not report retrieved dust lower than ~20 km above the surface, so the fitting scheme is inapplicable to them.

For comparison of the nightside and dayside tropical vertical dust distributions, Figures 4.13a-b show the zonal average dust density scaled opacity at 20°—25° N for all retrievals during MY 28 and MY 29 (including those from limb-staring observations) for the nightside and the dayside. (Note the decay in dust concentrations after the 2007 global dust storm during late southern summer of MY 28.) Figures 4.13c-d show the sampled longitudinal bins (colored red) to create the zonal averages. Outside of northern spring and summer, agreement between nightside and dayside zonal averages is generally good. For instance, just before southern summer solstice of MY 29, the vertical dust distribution on both the dayside and nightside resembles a profile of uniform mass mixing ratio up to 20 Pa with a density scaled opacity of  $8 \times 10^{-4} \text{ m}^2 \text{ kg}^{-1}$ . During the increase in dust concentration and depth of penetration during late northern summer of MY 29, nightside-dayside agreement is similarly good.

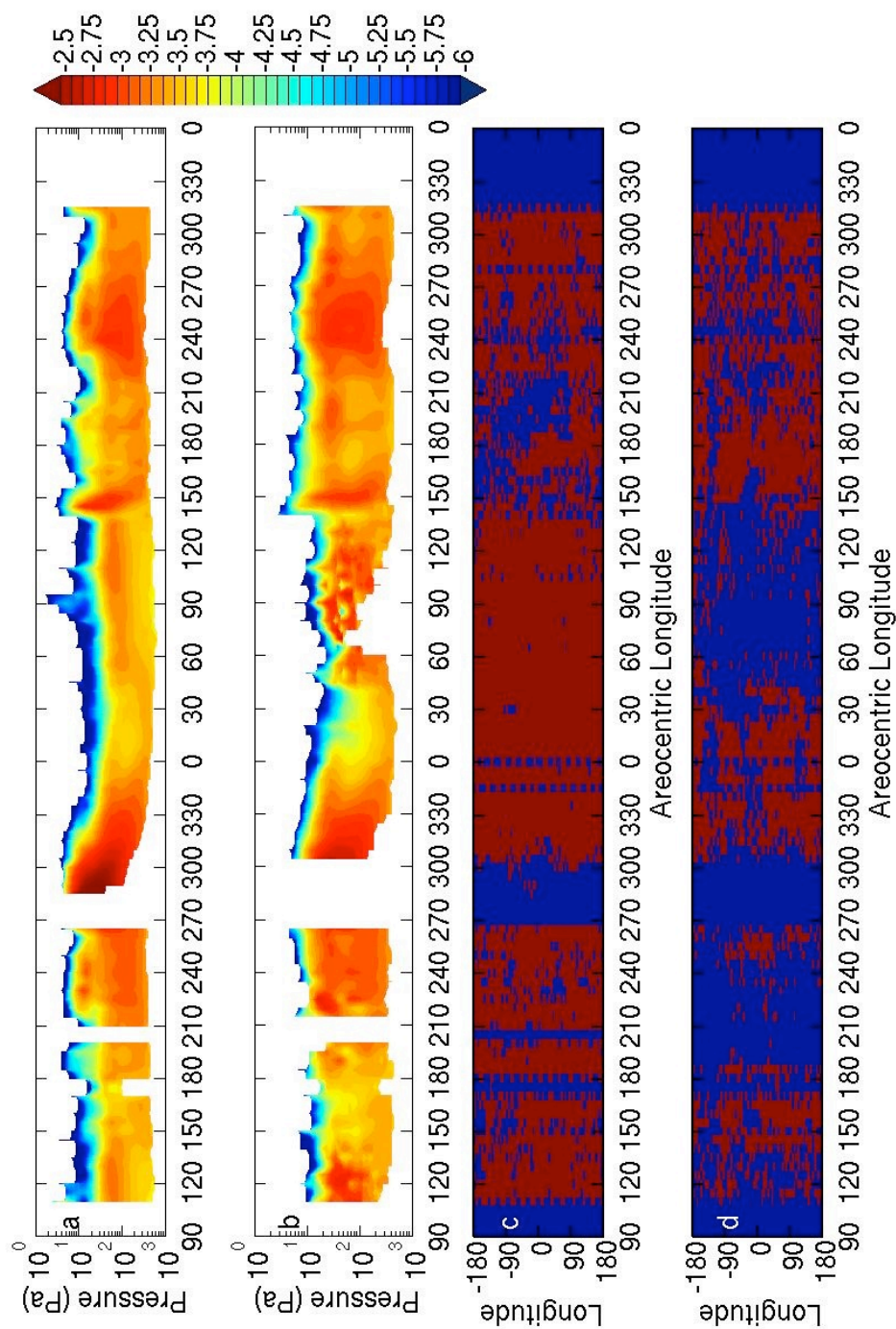


**Figure 4.13.** (a) Nightside log<sub>10</sub> zonal average dust density scaled opacity (m<sup>2</sup> kg<sup>-1</sup>) at 20°-25° N during MY 28 and 29; (b) Dayside log<sub>10</sub> zonal average dust density scaled opacity (m<sup>2</sup> kg<sup>-1</sup>) at 20°-25° N during MY 28 and 29; (c) Longitudinal sampling for (a): red indicates there is at least one successful retrieval in the longitudinal bin, blue indicates there are no retrievals in the longitudinal bin; (d) Longitudinal sampling for (b): red indicates there is at least one successful retrieval in the longitudinal bin, blue indicates there are no retrievals in the longitudinal bin.

In contrast to the rest of the year, the vertical dust distribution on the nightside around northern summer solstice of MY 29 has a maximum in density scaled opacity of  $6 \times 10^{-4} \text{ m}^2 \text{ kg}^{-1}$  at 60 Pa (a factor of three to four greater than nearer than the surface), while dust appears to be more uniformly mixed on the dayside. Longitudinal sampling (Figures 4.13c-d) is better on the nightside, and dust is not being retrieved to as low altitudes on the dayside as on the nightside, so the discrepancy could be attributed to profiles with high altitude dust maxima being preferentially unsuccessfully retrieved. For example, 424 retrievals are included in the nightside zonal average in this latitudinal band at  $L_s=90^\circ$  of MY 29, but there are only 11 retrievals contributing to the zonal average on the dayside.

Characteristic retrieval spacing at this latitude is  $\sim 1.8^\circ$ , there are thirteen orbits per day, and there are 11 days in the  $L_s$  bin, so we would expect  $\sim 400$  retrievals in the zonal average if all retrievals were successful. From Figure 4.3,  $\sim 90\%$  of individual profiles on the nightside in this bin contain a resolved maximum in dust density scaled opacity. Therefore, it is plausible that all retrievals with such a feature on the dayside were unsuccessful. Thus, in light of the good agreement in the vertical dust distribution between dayside and nightside retrievals during the rest of the year, there is likely a high altitude tropical dust maximum on the dayside.

### **4.5.2 Winter Polar “Dust”**

The decomposition of the vertical dust distribution presented in Chapter 4.4 also illuminates the high altitude ( $\sim 25 \text{ km}$ ) dust maximum within  $\sim 15^\circ$  of the south pole between  $L_s=45^\circ$  and  $150^\circ$ . The source of this dust is quite mysterious. On one hand,

advection and diffusion from elsewhere is unlikely, given the presence of the wide dust-clear region to its north. On the other hand, a local source is equally unlikely, since any dust deposited during the summer is frozen into carbon dioxide ice and inhibited from lifting.

A recent climatology of polar dust and water ice column opacities retrieved from TES nadir observations by *Horne and Smith* [2009] might resolve this conundrum. *Horne and Smith* [2009] shows that dust column opacities over both poles peak during the winter, that is, there is no apparent southern polar clearing region during northern spring and summer. Indeed, polar dust column opacities in the 9 micron band ( $1075 \text{ cm}^{-1}$ ) are  $>0.5$  within  $\sim 30^\circ$  of the south pole at the southern winter solstice. *Horne and Smith* [2009] attributes these high dust opacities to intense polar cap edge dust storm activity. Since present MCS retrievals usually do not report dust opacity below 8 km, the apparent dust-clear region in the southern extratropics could be the site of extremely intense and shallow dust storm activity, which then advects toward the pole. Retrievals from data early in the MCS mission that include nadir observations in the southern extratropics show the dust-clear region is in fact clear to the surface (N. Teanby et al., Vertical Profiles of Temperature and Dust from Mars Climate Sounder, paper presented at the 39<sup>th</sup> Meeting of the Division for Planetary Sciences of the American Astronomical Society, Orlando, FL, October 2007). Moreover, invoking shallow dust storms near the southern pole would not explain the peak in density scaled opacity at  $\sim 25$  km. However, a source of opacity not considered by *Horne and Smith* [2009] also could play a role.

The south polar high altitude dust maximum differs from the analogous equatorial and north polar pulses in relative magnitude.  $B$ , the parameter that measures the relative

magnitude of the pulse and dust density scaled opacity at  $\sim 8$  km) for these latter pulses ranges from 0.5 to 3, whereas  $B$  of 8—10 is typical in early summer for the south polar pulse. If summer equatorial water ice profiles were analyzed in the same way as we have analyzed dust,  $B$  of 10—20 might be expected. In other words, the dust maximum over the southern pole has a vertical distribution close to that of a detached condensate cloud. *Kleinböhl et al.* [2009] notices that MCS temperature retrievals near the southern pole in winter are very near the carbon dioxide frost point and in some cases cold enough to deposit carbon dioxide ice. Similarly supersaturated temperature profiles are present in both the TES and MGS Radio Science (RS) observations, which are thought to permit the formation of deep convective clouds [*Colaprete et al.*, 2008]. *Kleinböhl et al.* [2009] suggests that “small values of dust” retrieved near the winter pole by MCS may be due to carbon dioxide ice, which is highly scattering in much of the visible and infrared [*Forget and Pierrehumbert*, 1997], and avoids reporting opacity in profiles with temperatures below 150 K at the pressure level nearest the surface to minimize contamination of aerosol profiles by unretrieved carbon dioxide ice.

However, this filter may be imperfect, perhaps filtering out clouds near the surface through the lower atmosphere temperature criterion but passing through convective outflow clouds and similar detached cloudiness at higher altitudes. Thus, carbon dioxide clouds may be responsible for the south polar high altitude dust maximum. To test this hypothesis, the Convective Available Potential Energy with respect to carbon dioxide convection ( $CAPE_{CO_2}$ ) was calculated in each temperature retrieval:

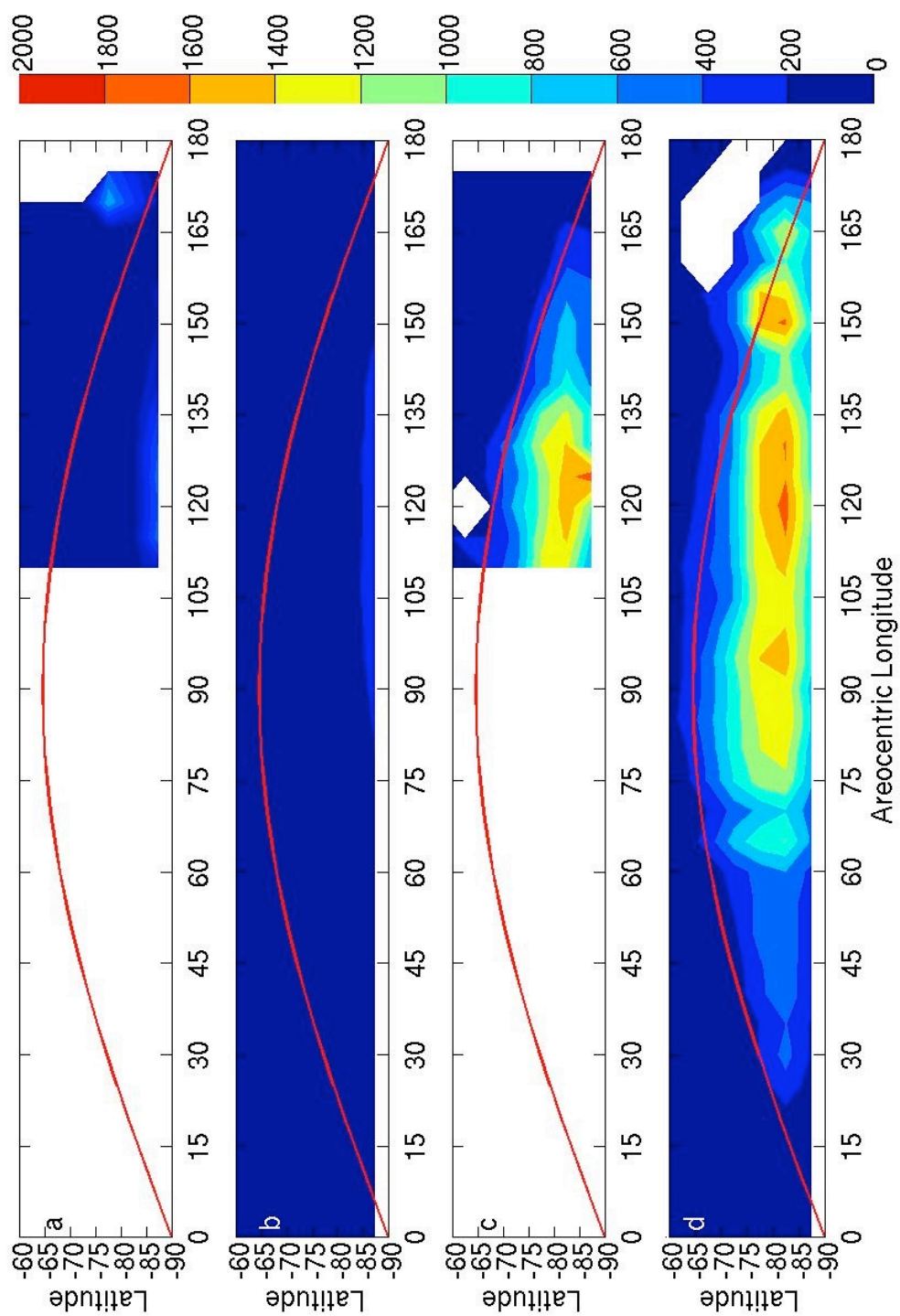


**Figure 4.14.** Latitudinal and seasonal variability in  $CAPE_{CO_2}$  ( $J kg^{-1}$ ) during northern spring and summer. (a) MY 28, nightside; (b) MY 29, nightside; (c) MY 28, dayside; (d) MY 29, dayside. The red line marks the northern edge of southern polar night.

$$CAPE_{CO_2} = \int_{Z_{LFC}}^{Z_{EQ}} g \frac{T_{sat} - T}{T} dz \quad (4.28)$$

where  $dz$  is the hydrostatic height coordinate,  $Z_{LFC}$  is the level of free convection (the lowest level at which the retrieval is supersaturated with respect to  $CO_2$ ),  $Z_{EQ}$  is the highest level at which the retrieval is supersaturated with respect to  $CO_2$ , and  $T_{sat}$  is the  $CO_2$  frost point.

Figures 4.14a-b show seasonal variability in zonally-averaged  $CAPE_{CO_2}$  near the south pole.  $CAPE_{CO_2}$  is much lower in nightside retrievals than dayside retrievals: an effect related to the viewing geometry and the strong horizontal temperature gradients near the pole in which the region nearest the pole contributes the greatest proportion of radiance to observations in which the pole is nearer than the tangent point of the limb than in which the pole is more distant than the tangent point of the limb. Thus, the pole appears colder when the instrument looks past it. One consequence of this effect is that near the north pole during northern winter,  $CAPE_{CO_2}$  is higher in nightside retrievals.

Dayside  $CAPE_{CO_2}$  is  $\sim 1000$  J/kg near the south pole during much of northern spring and summer, roughly correlating with the climatology of the southern polar high altitude dust maximum. Investigation of carbon dioxide cloudiness with MCS Level 1B data is an ongoing topic of research, but even at this point, I find it reasonable to attribute dust opacity retrieved from MCS observations to the south of the clearing region in the southern extratropics to the scattering effects of carbon dioxide ice rather than absorption of dust. Thus, much of the southern hemisphere of Mars is probably clear of dust during the winter.

### 4.5.3 Radiative-Dynamical Significance of the High Altitude Tropical Dust Maximum

The high altitude tropical dust maximum is of great dynamical interest, because the radiative heating profile it produces could differ significantly from what models presently assume. Recall that the diabatic heating and cooling rates due to an aerosol are proportional to its density scaled opacity or mass mixing ratio. The high altitude tropical dust maximum makes the vertical dust distribution of the atmosphere “top-heavy,” producing the strongest dust heating/cooling well above the surface. Since the mass mixing ratio at 20 km contributes much less to the column opacity than the mass mixing ratio near the surface, a “top-heavy” mass mixing ratio profile creates a higher rate of diabatic heating/cooling somewhere in Mars’s atmosphere than uniformly mixed dust, even for relatively low column opacities. Since GCMs and other models generally assume uniformly mixed dust to some height or decreasing mass mixing ratio with height profiles (“bottom-heavy” profiles), incorporating an equatorial dust pulse should produce a much different dust forcing in GCMs. In fact, this dust forcing has some analogy to the heating profile in the Earth’s tropics due to the release of latent heating by moist convection, which tends to peak 5-10 km above the surface [Tao *et al.*, 2001]. A few brief calculations underscore this point.

The visible heating rate,  $J$ , can be estimated as:

$$J = 7.3\varepsilon \frac{d_c \tau}{\rho} F_{in} \quad (4.29)$$

where 7.3 is the ratio between visible opacity and MCS A5 opacity,  $\varepsilon$  is the efficiency of absorption of solar radiation in the visible, and  $F_{in}$  is the incident solar radiation. Typical

tropical LLD is  $2.5 \times 10^{-4} \text{ m}^2 \text{ kg}^{-1}$ ,  $F_{in}$  at noon at the sub-solar point on Mars is  $\sim 500 \text{ W m}^{-2}$ , and  $\epsilon$  is minimally the additive inverse of the single scattering albedo, 0.05—0.1 and possibly somewhat higher. Thus, the heating rate then is  $\sim 4.5 \times 10^{-2}$ — $9.0 \times 10^{-2} \text{ W kg}^{-1}$  or 5.3—10.6  $\text{K sol}^{-1}$ . Typical tropical PD is a factor of 0.5—3 higher, producing zonally averaged heating rates within the pulse as large as  $\sim 30 \text{ K sol}^{-1}$  if skies above the dust haze are clear. (The effective heating rate in the equatorial pulse is proportional to LLD+PD due to the relatively deep mixing of dust at these latitudes).

The dust also will have an infrared heating and cooling effect, depending on the thermal structure of the atmosphere. During the day, lapse rates are strongly negative over the tropics, so that dust will tend to re-emit infrared radiation absorbed from the strongly heated surface at a somewhat lower temperature than the surface, producing net heating. In a more top-heavy dust distribution, there are higher concentrations of dust higher on the atmosphere (and therefore at a cooler temperature) relative to a uniformly mixed profile, so infrared heating, too, will be greater. At night, there is an inversion within 2 km of the surface [*Gierasch and Goody*, 1968], so the surface emits at fairly cool temperatures and any aerosol above the inversion (up to  $\sim 10 \text{ Pa}$ ) may re-emit at a higher temperature than the surface resulting in infrared cooling. (This pattern can be more complex, see *Schofield et al.*, 1997). To a first approximation in the optically thin case, the heating rate,  $dT/dt$ , due to this effect is:

$$\frac{dT}{dt} = \beta \frac{d_z \tau_{dust}}{\rho} \frac{\sigma(T_s^4 - T_r^4)}{c_p} \quad (4.30)$$

where  $\beta$  is a constant of proportionality of order unity (with respect to A5 channel density scaled opacity) related to the broadband infrared absorption convolved with the emission

temperature of the surface,  $T_s$ ,  $\sigma$  is the Stefan-Boltzmann constant, and  $T_r$  is the re-emission temperature of the dust. In the daytime,  $T_s$  is  $\sim 260$  K and  $T_r$  is  $\sim 200$  K in the high altitude tropical dust maximum, so the infrared heating at noon is  $\sim 10$  K  $\text{sol}^{-1}$ , assuming a high altitude tropical maximum with a density scaled opacity of  $5 \times 10^{-4} \text{ m}^2 \text{ kg}^{-1}$ . Thus, the visible and infrared heating are of similar magnitudes. At night, the cooling in the high altitude tropical dust maximum will be around  $-2$  K  $\text{sol}^{-1}$ .

So depending on the efficiency of dust absorption, a zonally and diurnally averaged heating rate of greater than  $10$  K  $\text{sol}^{-1}$  due to dust at  $20$  km above the surface is quite plausible in Mars's tropics. On the Earth, average latent heating rates at  $\sim 5$ — $10$  km altitude of  $5$ — $10$  K  $\text{day}^{-1}$  are observed in the convectively active tropical eastern and central Pacific [*Tao et al.*, 2001].

In northern spring and summer, Mars may have a tropical diabatic heating profile of magnitude and morphology quite similar to that of the Earth, differing only in its deeper penetration into the atmosphere. The high altitude tropical dust maximum at  $15$ — $25$  km will contribute diabatic heating to circulations less frictionally damped by the surface. And therefore at least qualitatively, the incorporation of the high altitude tropical dust maximum into models may produce a more vigorous lower atmospheric meridional circulation than presently simulated. Modeling by D. Tyler et al. (Dust Effects on Winds and Mixed Layered Depths, paper presented at the Mars Engineering Dust Workshop, Jet Propulsion Laboratory/NASA, Pasadena, CA, 18—19 March 2010) shows that incorporation of the high altitude tropical dust maximum into a modeled dust distribution enhances mixing within the convective boundary layer. A “top-heavy” dust distribution also may raise the condensation level of water ice simulated in models, enhancing

infrared heating due to water ice at higher altitudes in the atmosphere and may drive a more vigorous atmospheric circulation due to such forcing as simulated in part by *Wilson et al.* [2008]. Thus, to determine the extent to which the heating profile implied by MCS data drives a stronger circulation, GCM simulations with both prescribed dust and prescribed water ice distributions based on vertical information from MCS aerosol profiles likely will be necessary.

## 4.6 Summary

I have used MCS retrievals of temperature, dust opacity, and pressure to reconstruct the latitudinal-vertical distribution of dust during northern spring and summer and have developed a new framework for analyzing and representing the vertical distribution of dust in the atmosphere of Mars to describe its seasonal variability. Due to differences between day and night in the operation of the present retrieval algorithm, information about diurnal and interannual variability remains limited.

Yet the MCS dataset in northern spring and summer is sufficiently dense to show that:

1. Over much of the planet, the vertical dust distribution is not consistent with a physically plausible single parameter Conrath distribution.
2. Throughout most of northern spring and summer, the dust mass mixing ratio in the tropics tends to have a maximum at 15—25 km above the local surface. This maximum generally has a greater intensity and altitude in the northern hemisphere.

3. Similar maxima in mass mixing ratio sometimes occur near the north pole around the northern summer solstice.
4. Therefore, diabatic atmospheric heating due to dust in the tropical atmosphere of Mars may have a maximum at 15—25 km above the local surface. Heating rates (per mass) due to dust at this altitude are quite similar to heating rates in the tropical atmosphere of the Earth, where heating is mostly due to latent heat release from condensing water in moist convection.
5. Contrary to recent analysis of retrievals from TES data by *Horne and Smith* [2009], the south polar regions of Mars are effectively clear of dust during northern summer, while the north polar regions are nearly as dusty as the tropics. This dust-clear zone near the pole closely tracks the terminator and extends approximately twenty degrees in latitude equatorward of it.
6. The dust aerosol retrieved by MCS near the south pole throughout much of northern spring and summer has a vertical distribution similar to a condensate cloud and is very likely an artifact introduced by scattering from carbon dioxide clouds.
7. There was a significant increase in the depth of dust mixing throughout the tropics and mid-latitudes in MY 29 that greatly exceeded the depth of dust mixing observed in the same season during MY 28. This increase was coincident with “early season” tropical dust storm activity observed by THEMIS and MARCI in mid to late summer of MY 29. MY 28 is thought to have been a year without this type of dust storm activity.

These results introduce important new constraints on the radiative forcing in simulations by atmospheric models.

In Chapter 5, I will consider the implications of the high altitude tropical dust maximum for dust lifting and transport on Mars.

## Bibliography

Anderson, E. and C. Leovy (1978), Mariner 9 television limb observations of dust and ice hazes on Mars, *J. Atmos. Sci.*, *35*, 723-734.

Barnes, J.R. (1990), Possible effects of breaking gravity waves on the circulation of the middle atmosphere of Mars, *J. Geophys. Res.*, *95* (B2), 1401-1421.

Cantor, B., M. Malin, and K. S. Edgett (2002), Multiyear Mars Orbiter Camera (MOC) observations of repeated Martian weather phenomena during the northern summer season, *J. Geophys. Res.*, *107*(E3), 5014, doi:10.1029/2001JE001588.

Cantor, B. A., K. M. Kanak, and K. S. Edgett (2006), Mars Orbiter Camera observations of Martian dust devils and their tracks (September 1997 to January 2006) and evaluation of theoretical vortex models, *J. Geophys. Res.*, *111*, E12002, doi:10.1029/2006JE002700.

Chassefière, E., P. Drossart, and O. Korablev (1995), Post-Phobos model for the altitude and size distribution of dust in the low Martian atmosphere, *J. Geophys. Res.*, *100*(E3), 5525-5539.

Clancy, R. T., B. J. Sandor, M. J. Wolff, P. R. Christensen, M. D. Smith, J. C. Pearl, B. J. Conrath, and R. J. Wilson (2000), An intercomparison of ground-based millimeter, MGS TES, and Viking atmospheric temperature measurements: Seasonal and interannual variability of temperatures and dust loading in the global Mars atmosphere, *J. Geophys. Res.*, *105*(E4), 9553–9571.

Clancy, R. T., M. J. Wolff, and P. R. Christensen (2003), Mars aerosol studies with the MGS TES emission phase function observations: Optical depths, particle sizes, and ice cloud types versus latitude and solar longitude, *J. Geophys. Res.*, *108*(E9), 5098, doi:10.1029/2003JE002058.

Clancy, R.T., M.J. Wolff, B.A. Whitney, B.A. Cantor, M.D. Smith, and T.H. McConnochie (2009), Extension of atmospheric dust loading to high altitudes during the 2001 Mars dust storm: MGS TES limb observations, *Icarus*, *207*, 98-109, doi: 10.1016/j.icarus.2009.10.011.

Colaprete, A., J.R. Barnes, R.M. Haberle, and F. Montmessin (2008), CO<sub>2</sub> clouds, CAPE and convection on Mars: Observations and general circulation modeling, *Planet. Space Sci.*, *56*(2), 150-180, doi:10.1016/j.pss.2007.08.010.

Conrath, B.J. (1975), Thermal structure of the Martian atmosphere during the dissipation of the dust storm of 1971, *Icarus*, *24*, 36-46.

Forget, F. and R.T. Pierrehumbert (1997), Warming Early Mars with carbon dioxide clouds that scatter infrared radiation, *Science*, *278*, 1273-1276.

Forget, F., F. Hourdin, R. Fournier, C. Hourdin, O. Talagrand, M. Collins, S.R. Lewis, P.L. Read and J.-P. Huot (1999), Improved general circulation models of the Martian atmosphere from the surface to above 80 km, *J. Geophys. Res* *104*, 24155–24175.

Gierasch, P., and R. M. Goody (1968), A study of the thermal and dynamical structure of the Martian lower atmosphere, *Planet. Space Sci.*, *16*, 615-636.

Greeley, R., P.L. Whelley, R.E. Arvidson, N.A. Cabrol, D.J. Foley, B.J. Franklin, P.G. Geissler, M.P. Golombek, R.O. Kuzmin, G.A. Landis, M.T. Lemmon, L.D.V. Neakrase, S.W. Squyres, and S.D. Thompson (2006), Active dust devils in Gusev crater, Mars: Observations from the Mars Exploration Rover Spirit, *J. Geophys. Res.*, *111*, E12S09, doi:10.1029/2006JE002743.

Haberle, R.M., C.B. Leovy, and J.M. Pollack (1982), Some effects of global dust storms on the atmospheric circulation of Mars, *Icarus*, *50*, 322-367.

Haberle, R.M., J.B. Pollack, J.R. Barnes, R.W. Zurek, C.B. Leovy, J.R. Murphy, J. Schaeffer, and H. Lee (1993), Mars atmospheric dynamics as simulated by the NASA/Ames general circulation model I. The zonal mean circulation, *J. Geophys. Res.*, *98*, 3093-3124.

Hartogh, P., A.S. Medvedev, and C. Jarchow (2007), Middle atmosphere polar warmings on Mars: Simulations and study on the validation with sub-millimeter observations, *Planet. Space. Sci.*, *55* (9), 1103-1112.

Hinson, D.P., M. Pätzold, S. Tellmann, B. Häusler, and G.L. Tyler (2008), The depth of the convective boundary layer on Mars, *Icarus*, in press, doi:10.1016/j.icarus/2008.07.003.

Horne, D. and M.D. Smith (2009), Mars Global Surveyor Thermal Emission Spectrometer (TES) observations of variations in atmospheric dust optical depth over cold surfaces, *Icarus*, *200*(1), 118-128.

Jaquin, F., P. Gierasch, and R. Kahn (1986), The vertical structure of limb hazes in the Martian atmosphere, *Icarus*, 72, 528-534.

Kahre, M. A., J. R. Murphy, and R. M. Haberle (2006), Modeling the Martian dust cycle and surface dust reservoirs with the NASA Ames general circulation model, *J. Geophys. Res.*, 111, E06008, doi:10.1029/2005JE002588.

Kahre, M.A., J.L. Hollingsworth, R.M. Haberle, and J.R. Murphy (2008), Investigations of dust particle sizes in the martian atmosphere using the NASA Ames General Circulation Model, *Icarus*, 195, 576-597.

Kleinböhl, A., J. T. Schofield, D. M. Kass, W. A. Abdou, C. R. Backus, B. Sen, J. H. Shirley, W. G. Lawson, M. I. Richardson, F. W. Taylor, N. A. Teanby, and D. J. McCleese (2009), Mars Climate Sounder limb profile retrieval of atmospheric temperature, pressure, dust, and water ice opacity, *J. Geophys. Res.*, 114, E10006, doi:10.1029/2009JE003358.

Lee, C., W.G. Lawson, M.I. Richardson, N.G. Heavens, A. Kleinböhl, D. Banfield, D.J. McCleese, R. Zurek, D. Kass, J.T. Schofield, C.B. Leovy, F.W. Taylor, A.D. Toigo, (2009), Thermal tides in the Martian middle atmosphere as seen by the Mars Climate Sounder, *J. Geophys. Res.*, 114, E03005, doi:10.1029/2008JE003285.

Lee, S.W., P.C. Thomas, and J. Veverka (1982), Wind streaks in Tharsis and Elysium—Implications for sediment transport by slope winds, *J. Geophys. Res.*, 87, 10025-10041.

Leovy, C. (1982), Martian meteorological variability, *Adv. Space. Res.*, 2, 19-44.

Lewis, S. R., M. Collins, P. L. Read, F. Forget, F. Hourdin, R. Fournier, C. Hourdin, O. Talagrand, and J.-P. Huot (1999), A climate database for Mars, *J. Geophys. Res.*, *104* (E10), 24,177–24,194.

Malin, M. C., B. A. Cantor, T.N. Harrison, D.E. Shean and M.R. Kennedy. (2008), MARCI Weather Report for 10 November 2008-16 November 2008, MSSS Captioned Image Release #59.

Martin, L. J., and R. W. Zurek (1993), An analysis of the history of dust activity on Mars. *J. Geophys. Res.*, *98*, 3221-3246.

McCleese, D. J., J. T. Schofield, F. W. Taylor, S. B. Calcutt, M. C. Foote, D. M. Kass, C. B. Leovy, D. A. Paige, P. L. Read, and R. W. Zurek (2007), Mars Climate Sounder: An investigation of thermal and water vapor structure, dust and condensate distributions in the atmosphere, and energy balance of the polar regions, *J. Geophys. Res.*, *112*, E05S06, doi:10.1029/2006JE002790.

McCleese, D.J., J.T. Schofield, F.W. Taylor, W.A. Abdou, O. Aharonson, D. Banfield, S.B. Calcutt, N.G. Heavens, P.G.J. Irwin, D.M. Kass, A. Kleinböhl, W.G. Lawson, C.B. Leovy, S.R. Lewis, D.A. Paige, P.L. Read, M.I. Richardson, N. Teanby, and R.W. Zurek (2008), *Nature Geosci.*, *1*, 745-749, doi:10.1038/ngeo332.

Montmessin, F., F. Forget, P. Rannou, M. Cabane, and R. M. Haberle (2004), Origin and role of water ice clouds in the Martian water cycle as inferred from a general circulation model, *J. Geophys. Res.*, *109*, E10004, doi:10.1029/2004JE002284.

Rafkin, S.C.R., M.R.V. Sta. Maria, and T.I. Michaels (2002), Simulation of the atmospheric thermal circulation of a martian volcano using a mesoscale numerical model, *Nature*, 419, 697-699.

Richardson, M. I. (1998), Comparison of microwave and infrared measurements of Martian atmospheric temperatures: Implications for short-term climate variability, *J. Geophys. Res.*, 103(E3), 5911–5918.

Rind, D. and W.B. Rossow (1984), The Effects of Physical Processes on the Hadley Circulation, *J. Atmos. Sci.*, 41 (4), 479-507.

Schneider, E.K. (1983), Martian Great Dust Storms: Interpretive Axially Symmetric Models, *Icarus*, 35, 302-331.

Schofield, J.T., J.R. Barnes, D. Crisp, R.M. Haberle, S. Larsen, J.A. Magalhaes, J.R. Murphy, A. Seiff, and G. Wilson (1997), *Science*, 278 (5334), 1752-1758.

Smith, M.D. (2009), THEMIS Observations of Mars aerosol optical depth from 2002—2008, *Icarus*, 202(2), 444-452, doi:10.1016/j.icarus.2009.03.027.

Smith, M.D., J.C. Pearl, B.J. Conrath, and P.R. Christensen (2001), Thermal Emission Spectrometer results: Mars atmospheric thermal structure and aerosol distribution, *J. Geophys. Res.*, 106, 23929-23945.

Tao, W.-K., S. Lang, W. S. Olson, R. Meneghini, S. Yang, J. Simpson, C.

Kummerow, E. Smith and J. Halverson (2001), Retrieved vertical profiles of latent heat release using TRMM rainfall products for February 1998, *J. Appl. Meteor.*, *40*, 957-982.

Taylor, P.A., P.-Y. Li, D.V. Michelangeli, J. Pathak, and W. Weng (2007), Modelling dust distributions in the atmospheric boundary layer on Mars, *Bound. Lay. Met.*, *125* (2), 305-328.

Wang, J., and W.B. Rossow (1998), Effects of cloud vertical structure on atmospheric circulation in the GISS GCM, *J. Climate*, *11*, 3010-3029.

Wilson, R.J. and K. Hamilton (1996), Comprehensive model simulation of thermal tides in the martian atmosphere, *J. Atmos. Sci.*, *54*, 1290-1326.

Wilson, R. J., and M. I. Richardson (2000), The Martian atmosphere during the Viking mission, part I, Infrared measurements of atmospheric temperatures revisited, *Icarus*, *145*, 555–589, doi:10.1006/icar.2000.6378.

Wilson, R. J., S. R. Lewis, L. Montabone, and M. D. Smith (2008), Influence of water ice clouds on Martian tropical atmospheric temperatures, *Geophys. Res. Lett.*, *35*, L07202, doi:10.1029/2007GL032405.

Zurek, R.W., J.R. Barnes, R.M. Haberle, J.B. Pollack, J.E. Tillman, and C.B. Leovy (1992), Dynamics of the Atmosphere of Mars in H.H. Kieffer, B.M. Jakosky, C.W. Snyder, and M.S. Matthews, *Mars*, 1498 pp., University of Arizona Press, Tucson.